GEOSTATISTICAL ANALYSIS OF TEMPERATURE STRUCTURE IN THE ATMOSPHERIC BOUNDARY LAYER

By

BENJAMIN LYNN HEMINGWAY

Bachelor of Arts in Geography
University of Arizona
Tucson, Arizona
2010

Master of Science in Geography
Oklahoma State University
Stillwater, Oklahoma
2016

Submitted to the Faculty of the
Graduate College of the
Oklahoma State University
in partial fulfillment of
the requirements for
the Degree of
DOCTOR OF PHILOSOPHY
May, 2020

GEOSTATISTICAL ANALYSIS OF TEMPERATURE STRUCTURE IN THE ATMOSPHERIC BOUNDARY LAYER

Dissertation Approved:

Stephen J. Stadler

Committee Chair

Amy E. Frazier

Research Advisor

Adam J. Mathews

Brian R. Elbing

.

ACKNOWLEDGEMENTS

I am deeply grateful to my research advisor, Dr. Amy Frazier, for the encouragement, support, and mentorship over the years. I would not be where I am today if it were not for her. I would also like to thank my committee members, Dr. Brian Elbing, Dr. Steve Stadler, and Dr. Adam Mathews, for their guidance throughout this process. I would also like to acknowledge Dr. Jamey Jacob and the students and staff of the Unmanned Systems Research Institute (USRI) at Oklahoma State University (OSU). Without their technical support, my research, quite literally, would not have gotten off the ground. I am also very grateful to the School of Geographical Sciences and Urban Planning at Arizona State University (ASU) for being so welcoming and allowing me to be a visitor for the final two years of my Ph.D. program.

I would also like to express my gratitude for the generous financial support I have received throughout my time as a Ph.D. student. I am thankful to Dr. Jacob and the CLOUD-MAP project, funded by the National Science Foundation (NSF). Additionally, I am grateful for the funding I received through the NSF's Geography and Spatial Sciences Program in the form of a Doctoral Dissertation Research Improvement Grant (DDRI-1842715). I am also grateful to the OSU Graduate College and the OSU Foundation for awarding me the Distinguished Graduate Fellowship and the Holistic Science Award. These awards were particularly helpful in allowing me to continue my studies after my move to Arizona. I also wish to thank the OSU Department of Geography for their support in the form of the Robert and Lucy Fite Award.

Finally, I would like to acknowledge my wonderful family. Mom, without your support I could not have accomplished all that I have. To my parents-in-law, Mark and Linda, thank you for welcoming me into your family and making sure I continued the family tradition at OSU. I'm especially grateful to my wife, Allison, for putting up with me in graduate school all these years and for reading my papers. I am extremely grateful for my father, Daniel, an instrumental figure in my life who encouraged me to never give up on my passions. Lastly, I would like to thank Oliver for always being there at the end of the day. I couldn't have done it without you, bud.

Name: BENJAMIN LYNN HEMINGWAY

Date of Degree: MAY, 2020

Title of Study: GEOSTATISTICAL ANALYSIS OF TEMPERATURE STRUCTURE IN THE ATMOSPHERIC BOUNDARY LAYER

Major Field: GEOGRAPHY

Abstract: The lowest portion of the atmosphere, known as the atmospheric boundary layer (ABL), is of considerable importance to weather development at the local scale, but it is among the most difficult portions of the atmosphere to sample. The ABL is characterized by the presence of turbulence, which is the primary means by which heat and moisture are transported. Traditional monitoring techniques such as satellite technology, radar, and weather balloons are unable to sample the ABL at the spatial and temporal scales necessary to resolve the thermodynamic characteristics responsible for local weather development or monitor its rapidly changing structure. Over the past decade, small unmanned aircraft systems (sUAS) have emerged as a sensing methodology well suited to fill the spatio-temporal gaps left by the traditional atmospheric sensing technologies. While numerous studies have collected temperature and humidity data in the ABL, there has been almost no attention given to the determination of optimal spatial sampling strategies for capturing these variables. This research advances spatial science by applying geostatistical analysis techniques to a spatial, continuous random variable to a domain that has seen little attention by spatial scientists. The objective of this research is to apply geostatistics, principally, variogram analysis, to model the vertical spatial structure of thermodynamic variables (e.g., temperature) in the ABL using sUAS. The versatility of the variogram makes it ideally suited for modeling a continuous random variable whose spatial variation is influenced by turbulence. While the variogram was proposed in the 1940s to study turbulence in the spatial dimension, heretofore technology has generally precluded such an application in the ABL, with spatial dimensions instead being inferred from time series. The dynamic sensing capabilities of sUAS allow for an empirical assessment of the spatial structure of small-scale turbulence that, in turn, will allow for better parameterized climate models and weather forecasts.

TABLE OF CONTENTS

Chapter Page

I. INTRODUCTION 1

Project Motivation 1
Current State of Knowledge 2
The Atmospheric Boundary Layer 2
sUAS in Atmospheric Research 3
Boundary Layer Turbulence 4
Current Knowledge Gap 4
Research Objectives 5
Three Article Dissertation 6
References 7

II. VERTICAL SAMPLING SCALES FOR ATMOPHERIC BOUNDARY LAYER MEASUREMENTS FROM SMALL UNMANNED AIRCRAFT SYSTEMS 9

Introduction 9
Theory and Calculations 12
Study Site and Materials 15
Study Site and Data Collection 15
Platform 15
Sensors 16
Surface Weather Observations 16
Methods 17
Sample Variograms 17
Fitted Model Variograms 19
Obukhov Length Scale Calculation 19
Results 21
Flight Summaries 21
Variogram Modeling 23
Discussion 28
Conclusion 30
References 30

Chapter Page

III. HIGH RESOLUTION ESTIMATION AND SPATIAL INTERPOLATION OF TEMPERATURE STRUCTURE IN THE ATMOSPHERIC BOUNDARY LAYER USING A SMALL UNMANNED AIRCRAFT SYSTEM 34

Introduction 34
Theory 38
Materials and Methods 40
Study Area 40
Surface Weather Conditions at the Study Location 43
Radiosonde Measurements 43
Aircraft and Instrumentation 44
Calculation of Sonic Temperature 45
Estimating Sample Variograms 46
Fitting Model Variograms 47
Universal Kriging and Quantitative Assessment of Model Fit 47
Results 48
Profiles 48
Variograms 50
Cross-Validation of Kriging Estimates 53
Discussion 55
Resolution of Theorized Scaling and Model Fit 56
Profile Estimation Using Universal Kriging 58
Conclusion 58
References 59

Chapter Page

IV. ASSESING THE UNIVERSALITY OF THE TEMPERATURE STRUCTURE PARAMETER IN THE ATMOSPHERIC BOUNDARY LAYER 62

Introduction 62
Theory 65
Regionalized Variables 65
Obukhov Length 66
Experimental Design 68
Study Locations 68
Materials and Methods 72
Aircraft and Instrumentation 72
Data Collection 73
Data Analysis Methods 74
Results and Discussion 76
Variograms of Temperature Profiles 76
The Relationship Between C_c and z/L 77
Conclusion 84
References 84

V. CONCLUSION 88

Summary 88
Limitations and Future Considerations 90
Concluding Remarks 92
References 92

LIST OF TABLES

Table Page

2.1 Flight information and summary statistics.....21
2.2 Variogram results and fit diagnostics (RMSE) for all flights showing sill, range, and nugget values for temperature (Temp) and relative humidity (RH). 25
3.1 Flight times and maximum altitudes for the 12 profiles.....42
3.2 Variogram parameter estimates and fit diagnostic for Flights 1–6.....51
3.3 Variogram parameter estimates and fit diagnostic for Flights 1–3 (a) below 250 m AGL and (b) above 250 m AGL.....53
4.1 Flight start and end times 75

LIST OF FIGURES

Figure Page

2.1 Example of a typical variogram as a function of the lag distance showing the location of the nugget, range, and sill. 14
2.2 Location of Marena and Oklahoma State University Unmanned Aircraft Flight Station (OSU UAFS) 15
2.3 Location of iMet sensor placement on Iris+ sUAS platform. 16
2.4 Sample variogram displaying increasing scales of variability (scale domains) with distance. 18
2.5 Profile plots for (a) June 29 potential temperature, (b) June 29 relative humidity, (c) June 30 potential temperature, and (d) June 30 relative humidity 22
2.6 Sample variograms with Gaussian variogram models fit to (a) temperature and (b) relative humidity data from flight A3 on June 29. 24
2.7 Fitted Gaussian variogram models for (a) June 29 temperature, (b) June 29 relative humidity, (c) June 30 temperature, and (d) June 30 relative humidity. 25
2.8 Weather conditions at corresponding Mesonet stations for (a) temperature, (b) relative humidity, (c) pressure, and (d) wind speed. 26
2.9 Standardized variogram models for (a) June 29 temperature, (b) June 29 relative humidity, (c) June 30 temperature, and (d) June 30 relative humidity. 28
2.10 Sample variograms of (a) Flight A5 on June 29 and (b) B6 on June 30 (b). 29
3.1 Map of the Moffat flight location in the San Luis Valley 41
3.2 Surface weather conditions at the Moffat flight location, measured approximately 3 m AGL. 42
3.3 Radiosonde potential temperature [Θ] and wind speed profiles. 43
3.4 DJI Matrice 600 hexacopter outfitted with a Young Model 81000 ultrasonic anemometer on top 44
3.5 Temperature profiles captured by sUAS (colored lines) and radiosondes (black lines). 49
3.6 Sample variograms (circles) and fitted 2/3 power law model variograms (red lines) for all full profiles 50
3.7 Sample variograms (points) and fitted 2/3 power law model variograms (lines) for 0708, 0759, and 0859 profiles for altitudes above and below 250 m AGL 52
3.8 SDR profiles of kriging estimates (grey lines) and smoothing splines (red lines). Dashed lines are the ideal ratio of 1. 54
4.1 Oklahoma Mesonet sites and ecoregions visited. 69
4.2 1:50,000 aerial photos of the six Oklahoma Mesonet sites 71

Figure Page

4.3 R.M. Young Model 81000 ultrasonic anemometer with Oklahoma Mesonet tower in background. 73
4.4 Sample variograms (points) from (a) Arnett Flight 1 and (b) Goodwell Flight 3. Power law model variogram with α fixed to 2/3 fit to sample variogram (b). 77
4.5 C2 as a function of z/L 78
4.6 Meteogram of conditions at the Arnett site 80
4.7 Meteogram of conditions at the Bixby site. 80
4.8 Meteogram of conditions at the Fairview site 81
4.9 Meteogram of conditions at the Goodwell site 81
4.10 Meteogram of conditions at the Lane site. 82
4.11 Meteogram of conditions at the Marena site 82

CHAPTER I

INTRODUCTION

Project Motivation

This doctoral dissertation research seeks to identify proper spatial sampling scales for geostatistical analysis techniques for atmospheric boundary layer (ABL) research using small unmanned aircraft systems (sUAS). Using those findings in combination with variogram analysis, this research will then identify the size, shape, and uniformity of coherent turbulence structures, which will make a fundamental contribution to the current understanding of small-scale atmospheric turbulence. Data and results were shared with National Severe Storm Laboratory (NSSL) forecasters to improve severe storm detection and warnings. Thus, this doctoral dissertation research will contribute geostatistical methods for atmospheric sampling, spatial science theory for understanding small-scale turbulence, and contribute novel data streams for real-world, severe weather forecasting applications.

Recent technological advancements in unmanned and autonomous systems have fostered the increasing use of sUAS in meteorology and atmospheric sciences. The versatility of sUAS make them well suited for filling spatial and temporal sensing gaps in the ABL, which is the portion of the atmosphere in direct contact with the surface of the earth and a critical area for weather development including severe local storms. However, we currently do not have established sampling methodologies or a universal understanding of the scales associated with

the atmospheric processes operating within this region to guide those sampling schemes. Building on small-scale turbulence theories from Kolmogorov (1941) and Obukhov (1949) along with established spatial analytical methods from geography and the spatial sciences, this research will develop the spatial sampling strategies needed for efficient and effective sampling of scaler variables in the ABL and develop analytical methods for uncovering the processes impacting weather development in the ABL.

Current State of Knowledge

The Atmospheric Boundary Layer

The lowest portion of the atmosphere, known as the atmospheric boundary layer (ABL) or planetary boundary layer for its proximity to the earth's surface, is of considerable importance to weather development at the local scale. Thermodynamic characteristics of this lower portion of the atmosphere are very different compared to the rest of the atmosphere (e.g., troposphere, stratosphere, etc.). Heavily influenced by its contact with the earth's surface, ABL conditions can change over time spans as short as one hour (Stull 1988). Primarily, diurnal temperature fluctuations caused by radiation absorption and emission by the earth's ground surface provide the source of energy driving circulation, which changes the state of the ABL, sometimes over short time intervals. These changes in the atmospheric state (e.g., temperature, humidity, etc.) are distributed by transport processes, chiefly turbulence.

Researchers have long known that the ABL is an important region for weather development and turbulence, but it is among the most difficult portions of the atmosphere to sample. Traditional atmospheric monitoring techniques such as satellite technology and weather balloons suffer limitations, particularly at smaller (spatial and temporal) scales. Radar revolutionized weather forecasting, particularly with the inception of NEXRAD Doppler radar in 1988 (Doviak and Zrnic 1993); however, the radar signal can be blocked by terrain and the curvature of the earth, resulting in coverage gaps. Additionally, radar is not able to directly sense thermodynamic variables, such as

temperature, which are critical for understanding weather development. Satellite based remote sensing technologies, such as the Geostationary Operational Environmental Satellite (GOES), have been instrumental in weather observation and forecasting for decades, however, the relatively coarse spatial resolution (500 m to 2 km depending on the spectral band) of the instruments onboard these satellites make them unsuitable for sensing atmospheric phenomena smaller than the mesoscale, while cloud cover aloft can obscure phenomena near the ground. Traditional in situ methods also suffer limitations. Weather balloons are launched twice daily from a sparse network of locations around the world, but the sensors carried by the balloons only capture a handful of measurements within the ABL due to the rapid rate of ascent, and the radiosonde transponders are not able to be controlled or recovered. Sensors onboard manned aircraft are able to collect data at higher spatial and temporal resolutions, but aircraft are expensive and dangerous to operate near the ground in the ABL, and manned aircraft are not ideal for situations in which severe weather is developing.

sUAS in Atmospheric Research

In the past decade, sUAS have emerged as a supportive sensing technology well suited to fill the spatial and temporal gaps left by the alternative traditional atmospheric sensing technologies discussed above. The use of sUAS in the geosciences has increased dramatically in recent years, particularly for image acquisition, due to their low cost and versatility (Singh and Frazier 2018). This rapid adoption prompted the Federal Aviation Administration (FAA) to formalize regulations pertaining to the operation of sUAS for research purposes in Part 107 of the Federal Aviation Regulations. Similar regulations have been enacted by the European Aviation Safety Agency (EASA), which will facilitate the expanded use of the new technology.

The benefits of sUAS are not limited to remote sensing imagery applications, however. Atmospheric scientists have found that they are a powerful tool for in situ sampling of the ABL. While there have been numerous studies collecting temperature and humidity data in the ABL (e.g., Mayer et al. 2012; Cassano et al. 2014; Higgins et al. 2018) there has been almost no attention given to the determination of optimal spatial sampling strategies for capturing these variables. Determining

the optimal distance (i.e., scale) at which to collect samples based on the dissipation of autocorrelation is necessary to ensure adequate capture of the measured variable. The necessary spatial distance between samples collected from a single sUAS vehicle, and correspondingly, the necessary distance between multiple vehicles performing coordinated sampling, is currently uncertain. A better understanding of coherent turbulent structures, as captured through variation in thermodynamic variables such as temperature, will allow for better informed sampling, enhanced mission planning, and improved scientific analyses.

Boundary-Layer Turbulence

Turbulence is an important process for understanding severe weather formation (e.g., tornadoes) because it is responsible for vertical transport in the ABL, whereas wind is the primary cause of horizontal transport, known as advection (Stull 1988). Turbulence is prevalent in the ABL and is generated from buoyancy due to temperature variations or wind shear. It is characterized by a superposition of swirls, called eddies, that scale in size from the approximate ABL thickness (~1 km) down to only a few millimeters. Richardson (1922) proposed the concept of an energy cascade, where kinetic energy enters the largest turbulent eddies. Unstable and influenced by the current boundary layer condition, these eddies break up and their energy is transferred to smaller eddies. This process continues until turbulent motions become small, and the energy dissipates through viscous forces, typically at the scale of only a few millimeters (Pope 2000). Kolmogorov (1941), for whom these smallest scales are named, proposed several hypotheses regarding the structure of the small-scale turbulent eddies. However, these hypotheses remain difficult to validate for the ABL because heretofore technologies were not available to test them in the ABL.

Current Knowledge Gap

sUAS afford more dynamic sensing capabilities in the ABL, however, the new technology has outpaced the development of spatial sampling theory necessary to best capture the complicated physical processes in the ABL. Fluctuation in turbulent intensities are known to correspond to fluctuations in discernment of scaler variables such as temperature and humidity, or gas

concentrations (e.g., pollutants) (Stull 1988). Understanding of the size and shape of turbulent eddies is essential to effectively and efficiently sample in the ABL. The spatial scales of these eddies have historically been determined by applying Taylor's (1938) frozen turbulence hypothesis, which depends on the assumption that turbulent eddies are "frozen" as they advect past a sensor, thus allowing the local change within each eddy to be negligible. Researchers have used this theory to take measurements at one point in space for a period of time as the eddies advect past the sensor. The mean wind speed is then used to translate the time series into spatial dimensions. However, this method is disadvantageous because inferring spatial dimensions relies on the validity of the hypothesis. To date scientists have not collected evidence to suggest turbulence eddies remain fixed even for short time intervals, and continue to face challenges when trying to capture a spatial snapshot of the ABL sufficiently large enough to fully define its spatial structure.

Research Objectives

Geostatistics, specifically the variogram, offers a viable means for quantitatively describing the spatial structure of variables whose spatial positioning is influenced by turbulent motions. Geostatistics is a branch of statistics that is suited for the analysis of spatially autocorrelated (and often spatial nonstationary) data. The variogram, a key component of geostatistical theory, is a function that describes the degree of spatial autocorrelation. Indeed, the variogram was originally developed to study turbulent flows (Kolmogorov 1941) and described as a "structure function" by Obukhov (1949).

Geostatistical theory developed outside of turbulence studies in the decades that followed, primarily in geology, but also with contributions from practitioners in forestry and meteorology (Cressie 1990). Geostatistical methods have been widely applied in the terrestrial geosciences, but has seen limited use outside of the variogram (structure function). This is likely a result of limited spatial sampling capabilities. The variogram has been applied to temperature data collected in the ABL from aircraft and from balloon measurements, but has not been widely applied in the atmospheric sciences.

In situ spatial sampling in the ABL has been challenging leading to the ubiquitous use of tower instrumentation and while the structure function has seen use, it has generally been applied to temporal data. The dynamic sensing capabilities offered by sUAS provide the ability to spatial sample the ABL like never before. With increased spatial sampling capabilities, geostatistical methods can be more widely applied. Such methods go beyond the parametric estimation of temperature structure through the variogram, but include ways to handle spatial nonstationarity and also predict unknown quantities at unsampled points while simultaneously receiving a measure of uncertainty through the mean squared prediction error (Cressie and Zimmerman 1992). Given the available toolkit of theory and sampling methods, the objective of this research is to apply geostatistics, principally, variogram analysis, to model the vertical spatial structure of thermodynamic variable (e.g., temperature) in the ABL using sUAS. Three specific objectives, each pursued in the form of an independent research article, are outlined below.

Three Article Dissertation

The first article identifies minimum sampling scales for temperature and relative humidity measurements in the ABL. sUAS provide a dynamic sensing platform to capture thermodynamic variables in the ABL, however, research on the vertical sampling scales for collecting atmospheric measurements from sUAS and the variabilities of these scales across atmospheric phenomena (e.g., temperature and humidity) is needed. The objective of this study is to use variogram analysis, a common geostatistical technique, to determine optimal spatial sampling scales for two atmospheric variables (temperature and relative humidity) captured from sUAS. Results show that vertical sampling scales of approximately 3 m for temperature and 1.5–2 m for relative humidity were sufficient to capture the spatial structure of these phenomena under the conditions tested. Future work is needed to model these scales across the entire ABL as well as under variable conditions. This research was published in *Atmosphere* (Hemingway et al. 2017).

The second article contributes to the understanding of the small-scale vertical structure of temperature at separation distances inherent to the inertial range of turbulence. Structure functions are

estimated from vertical profiles of temperature collected using an ultrasonic anemometer mounted on an sUAS. Using geostatistical methodologies specifically developed for spatially nonstationary and spatially dependent random variables, temperature structure was estimated from six profiles reaching roughly 500 m in altitude. A mean function was specified to account for the variation in temperature with altitude and the structure function was estimated from the residuals. A 2/3 scaling exponent was fit to the resulting curves commensurate with the inertial range of turbulence. The resulting structure functions of residuals were able to resolve the inertial range of turbulence on most profiles at a range of separation distances. It was found that geostatistical methods for spatially nonstationary random variables were well suited in certain cases to describe the vertical structure of temperature in the ABL. The results of this research have been accepted for publication in *Boundary-Layer Meteorology* (Hemingway et al. in press)

The third article assesses the universality of the temperature structure parameter in the power law variogram model that describes the intensity of the spatial variation. Statistical properties of turbulent quantities in the ABL are hypothesized to be a universal function of a stability parameter and not vary based on the nature of the surface. To test this hypothesis, the second-order statistical quantity (the temperature structure parameter) of the power law relationship in the inertial range was estimated from numerous profiles of temperature across various ecoregions of Oklahoma. The results of this study are to be submitted to *Environmental Fluid Mechanics* in the summer of 2020. *Environmental Fluid Mechanics* features basic and applied articles about natural fluid systems and would be an appropriate outlet for this research.

References

Cassano, J.J. (2014). Observations of atmospheric boundary layer temperature profiles with a small unmanned aerial vehicle. *Antarctic Science, 26*(2), 205–213.

Cressie, N. (1990). The origins of kriging. *Mathematical geology*, *22*(3), 239–252.

Cressie, N., & Zimmerman, D. L. (1992). On the stability of the geostatistical method. *Mathematical Geology*, *24*(1), 45–59.

Doviak, R.J.; Zmic, D.S. (1993). Doppler Radar and Weather Observations, 2nd ed: Academic Press, San Diego

Hemingway, B.L., Frazier, A.E., Elbing, B.R., & Jacob, J.D. (2017). Vertical sampling scales for atmospheric boundary layer measurements from small unmanned aircraft systems (sUAS). *Atmosphere*, *8*(9), 176.

Hemingway, B.L., Frazier, A.E., Elbing, B.R., & Jacob, J.D. (2020). High-resolution estimation and spatial interpolation of temperature structure in the atmospheric boundary layer using a small unmanned aircraft system. *Boundary-Layer Meteorology*, (in press).

Higgins, C.W., Wing, M.G., Kelley, J., Sayde, C., Burnett, J., & Holmes, H.A. (2018). A high resolution measurement of the morning ABL transition using distributed temperature sensing and an unmanned aircraft system. *Environmental Fluid Mechanics*, 18(3), 683–693.

Kolmogorov A.N. (1941). Local structure of turbulence in an incompressible fluid for very large Reynolds numbers. *Dokl Akad Nauk SSSR* 30: 299–303.

Mayer, S., Sandvik, A., Jonassen, M.O., & Reuder, J., (2012). Atmospheric profiling with the UAS SUMO: A new perspective for the evaluation of fine-scale atmospheric models. *Meteorol. Atmos. Phys*. 116, 15–26.

Obukhov, A.M. (1949). Structure of the temperature field in turbulent flow. *Geogr i Goofiz* 2(1): 58–69.

Pope, S. (2000). *Turbulent flows*. New York: Cambridge University Press.

Richardson, L.F. (1922). *Weather prediction by numerical process*. New York: Cambridge University Press.

Stull, R.B. (1988). *An introduction to boundary layer meteorology*. Dordrecht: Kluwer Academic Publishers.

Taylor, G.I. (1938) The spectrum of turbulence. *Proc R Soc London Ser A 164*: 476–490.

CHAPTER II

VERTICAL SAMPLING SCALES FOR ATMOSPHERIC BOUNDARY LAYER MEASUREMENTS FROM SMALL UNMANNED AIRCRAFT SYSTEMS

Introduction

The atmospheric boundary layer (ABL) is the lowest portion of the earth's atmosphere and plays an important role in the formation of weather phenomena (Stull 1988). The ABL is the portion of the troposphere in direct contact with the surface of the earth, approximately 1 km thick on average, where there is a considerable exchange of energy between the two systems that can impact local weather events on time scales as small as one hour (Stull 1988). Simple meteorological measurements collected from within the ABL, including thermodynamic variables such as temperature, pressure, and humidity, and kinematic variables such as wind velocity, are key to understanding this exchange of energy (Mayer et al. 2012) and the role it plays in the formation of severe weather events such as thunderstorms and tornadoes. Low altitude sampling would allow for measurement of surface-based convergence and the intersection of airmass boundaries (Ladue et al. 2010), both of which would aid in the understanding of tornadogenesis. With the possibility of rotation occurring in as few as twenty minutes from the first sign of possible tornadic activity (Frew et al. 2012), rapidly-deployable, low altitude platforms that can collect measurements at fine spatial and temporal scales can lead to timelier and more precise tornado warnings (Ladue et al. 2010; Frew et al. 2102). However, these types of measurements are not readily available from the existing suite of meteorological surveillance tools.

Networks of ground weather stations (i.e., mesonets) were first constructed in the U.S. during the late-20th century to observe mesoscale meteorological phenomena. Ground stations typically consist of a tower, commonly about 10 m high, equipped with various atmospheric sensors to capture pressure, temperature, humidity, wind velocity, and other environmental data (McPherson et al. 2007). Towers are usually spaced between 2–40 km apart, which allows measurements to be interpolated over regional extents, but sampling occurs at very low altitudes (lower than 10 m), and thus mesonet towers are not able to capture the full dynamics of the ABL. Weather balloons (i.e., sounding balloons) allow for sensing of the full vertical profile of variables in the ABL, but their sampling altitude is limited by the length of their tethers, and non-tethered balloons make uncontrolled ascents limiting the derived conclusions from their sampling. Further, the radiosondes that capture the data onboard the balloon are often lost and cannot be controlled from the ground (Konrad et al. 1970).

With the limitations of ground-based weather monitoring technologies, investments in remote weather-sensing satellites over the past several decades have led to considerable advancements in weather forecasting and monitoring. However, satellite systems remain unable to provide the spatial precision, temporal resolution, and/or specific types of data needed for local meteorological observations in the ABL (Frew et al. 2012). In particular, the Geostationary Operational Environmental Satellite (GOES) system has been a centerpiece of weather forecasting in the U.S. (Jensen 2015). Since the first launch in 1975, GOES has been deployed on various satellite platforms for weather forecasting, severe storm tracking, and meteorology research. However, the coarse spatial resolution of the imager is not sufficient to observe phenomena at the micro scale—defined as less than 1 km (Stull 1988)—which is the scale at which atmospheric processes contributing to the formation of severe local storms occur (Frew et al. 2012).

Simultaneous to developments in weather satellite technology, weather services began incorporating weather surveillance radar (WSR) technology into forecasting and storm tracking

beginning in the 1950s (Doviak and Zrnic 1993). Weather radars work by sending directional pulses of microwave radiation from a radar station and measure the reflectivity, or amount of radiation scattered by water droplets or ice particles back to the sensor (Doviak and Zrnic 1993). While radar systems such as the current WSR-88D radar network (NEXRAD) are able to somewhat fill the measurement gaps between ground-based tower measurements and satellite sensors, they are limited in the type of meteorological information they can collect, particularly thermodynamic data such as temperature and humidity. Additionally, weather radars have difficulty sensing the ABL due to the curvature of the earth and obstructions such as buildings or mountainous terrain (LaDue et al. 2010; Bendix et al. 2017). There can also be interference from other phenomenon such as birds, insects, and ground clutter (Chowdhury et al. 2016; Farnsworth et al. 2016; Golbon-Haghighi et al. 2016).

Given the limitations of ground-based weather stations, satellite sensors, and ground radar for capturing measurements in the ABL, alternative technologies are needed. Small unmanned aircraft systems (sUAS) are a rapidly emerging technology that have the potential to fill the aforementioned spatio-temporal gaps in atmospheric sampling (Frew et al. 2012; Frazier et al. 2017). In the U.S., a sUAS is defined as weighing less than 25 kg (55 lbs.) and may be of either fixed-wing or rotor-wing platform. A plethora of sensors and platforms are available (see Elston et al. (2015) for a review). While sUAS have been increasingly employed in ABL sampling over the last several years their use dates back to at least 1970 when Konrad et al. (1970) used a sUAS to capture temperature, humidity, pressure, and aircraft velocity at altitudes up to 3,048 m (10,000 ft.). More recently, sUAS have been used to successfully capture atmospheric measurements such as temperature profiles in Antarctica during various mixing conditions (Cassano 2014), validate fine-scale atmospheric models in Iceland (Mayer et al. 2012) and compare temperature and relative humidity measurements to radiosondes in New Zealand (Cook et al. 2013). Additionally, they have been utilized in capturing data in supercell storms (Roadman et al. 2012) and air masses (Houston et al. 2012).

While the use of sUAS for sampling the ABL has increased in recent years, little research has been conducted on the optimal vertical spatial scales for collecting measurements and whether these scales vary across atmospheric phenomena (e.g., temperature and humidity). Most natural phenomena display spatial autocorrelation, that is, samples collected near each other in space are more likely to be similar than samples captured at further distances. Knowledge of the scales (temporal and/or spatial) over which a given phenomenon is correlated provides insight into the coherent structures within the flow, which in turn provides insight into how we can most efficiently sample the environment. A "more is always better" approach may not be optimal, as there may become a point when no new information is returned with increasing numbers of samples (Bolstad 2005). This type of collection efficiency is particularly critical for sUAS because there are large variances in communication rates, link reliability, mesh network connectivity, and bandwidth (Crick and Pfeffer 2003) with UAS data capture, and storage devices must be miniaturized to fit payload requirements.

The objective of this study is to use common geostatistical techniques to determine vertical spatial sampling scales for two atmospheric variables (in this case temperature and relative humidity) captured from sUAS. Specifically, variogram modeling, a geostatisitical technique that can quantify the spatial autocorrelation of a given signal (Isaaks and Srivastava 1989), is used to capture the spatial structure of these atmospheric phenomena at different times of the day. Analysis of the variogram provides guidance on the distance over which the given data become incoherent (i.e., spatial autocorrelation dissipates), providing a measure of the optimal spatial separation to allow between measurements collected from sensors onboard sUAS. Ultimately, this type of information will aid in mission planning, address data storage limitations, and allow for more advanced geostatistical analyses of these atmospheric phenomena.

Theory and Calculations

The processes that shape the atmosphere, much like Earth processes, are governed by physical laws, and are thus deterministic in nature. However, the many forces influencing the

spatial variation of a particular atmospheric property combined with the nonlinearity of the governing equations makes the behavior appear random. This makes deterministic mathematical models for describing the spatial relationship between two sample points impractical.

Consequently, a probabilistic approach is required for modeling the behavior. Such a variable is known as a regionalized variable and is best described using a random function. Although the spatial variation in the regionalized variable may appear to be the result of a stochastic process, there is still an inherent structure to that variable, and the values may have a statistical relationship relative to their location in space (Burrough et al. 2015). The random function can be modeled by

$$Z(x) = \mu + \varepsilon(x) \tag{2.1}$$

where $Z(x)$ is the observation, μ is the mean of the process that is assumed spatially uniform, and $\varepsilon(x)$ is a random quantity with a mean of zero. The expected difference in values between the variable at two locations is

$$E[Z(x) - Z(x+h)] = 0 \tag{2.2}$$

where $Z(x)$ is the value of the variable at location x and $Z(x+h)$ is the value at location $x+h$, and h is a spatial separation distance. The variation between the two locations can be assumed to be a function of their spatial separation. The variance of the difference can then be used to measure the spatial relationship using

$$E[\{Z(x) - Z(x+h)\}^2] = 2\gamma(h) \tag{2.3}$$

where $2\gamma(h)$ is the variogram γ is known as the semivariance.

The equation to compute the experimental variogram from sample data is

$$\hat{\gamma}(h) = \frac{1}{2N(\mathrm{h})}\sum_{i=1}^{N(\mathrm{h})}\{z(x_i) - z(x_i+h)\}^2 \tag{2.4}$$

where $z(x_i)$ is the observed value of z at location xi separated by distance h, and n is the number of sample pairs (Oliver and Webster 2015). From the variogram plot, the distance at which spatial dependence of the regionalized variable is no longer present can be determined through analysis

of three properties: the range, sill, and nugget (Figure 2.1) The upper bound of variogram values is referred to as the sill, which occurs when the measured values between samples are invariant at larger lag distances, and the curve of the variogram levels off. The lag distance at which the sill occurs is known as the range, so-called because this is the range at which the measured attributes have spatial dependency. In certain instances, the variogram model may not pass through the origin but instead intersect the ordinate at γ greater than zero. While it is reasonable to expect that the variogram would be zero at a separation distance of zero, there still is uncertainty in the data, and this phenomenon is known as the nugget effect.

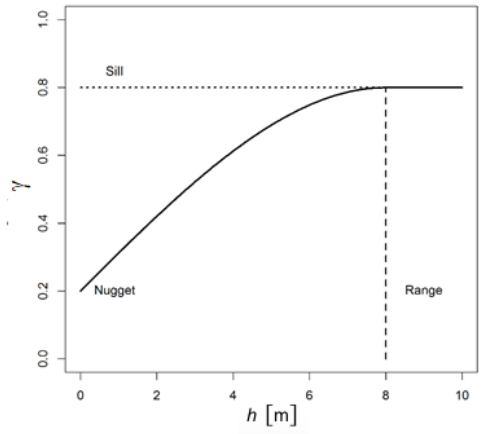

Figure 2.1. Example of a typical variogram as a function of the lag distance showing the location of the nugget, range, and sill.

There are certain considerations to be made prior to modeling the variogram. A large enough sample is needed to ensure reliability. Oliver and Webster (2015) suggest a sample size of no fewer than 100 observations. Additionally, careful consideration should be used when selecting size of the distance of the separation bins. A spacing that is too large will likely result in a variogram that is flat or does not capture the true spatial structure of the phenomenon. Distance bins that are too small for the given sample size can result in a noisy variogram (Oliver and Webster 2015) which can obscure observation of the physical process under investigation. For

non-systematic sampling schemes, such as in this study, the average sample spacing can serve as a good starting point for the distance bins (Isaaks and Srivastava 1989).

Study Site and Materials

Study Site and Data Collection

Flights took place over two days in June 2016 at two sites in central Oklahoma, USA Figure 2.2). On June 29, 2016, data were collected at the Marena Mesonet site located near Coyle, OK (36° 3' 51" N, 97° 12' 45" W, at an elevation of 327 m above mean sea level [MSL]). Rural grasslands with small patches of forest surround the site. On June 30, 2016, data were collected at Oklahoma State University's Unmanned Aircraft Flight Station (UAFS) near Ripley, OK (36° 9' 44" N, 96° 50' 9" W at an elevation of 319 m MSL). The UAFS is also located in a rural area surrounded by farmland, grassland, and small forest patches. Central Oklahoma is characterized by a humid subtropical climate, and experiences hot, humid summers and cool winters. On both flight days, conditions were clear with minimal cloud cover.

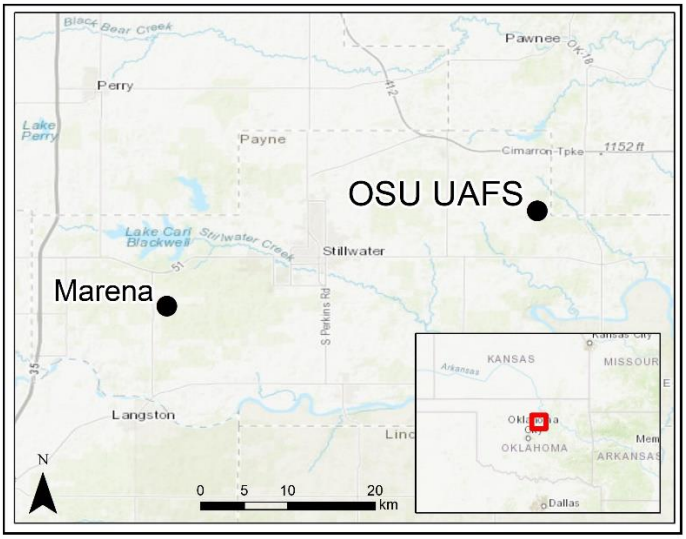

Figure 2.2. Location of Marena and Oklahoma State University Unmanned Aircraft Flight Station (OSU UAFS).

Platform

The sUAS platform used for data collection was a 3DR Iris+ (3D Robotics, Inc., Berkeley, CA) multirotor aircraft (Figure 2.3). The Iris+ weighs 1,282 g and is 550 mm in

diameter from rotor tip-to-tip. It has a payload of 400 g, and the lithium polymer battery provides up to 22 minutes of flight time under favorable conditions. The Iris+ sUAS is controlled by an onboard autopilot and is capable of autonomous flight through control via a ground control station through radio frequency communication at 915 MHz.

Sensors

The iMet XQ sensor (International Met Systems, Grand Rapids, MI) was used to collect atmospheric measurements. It is a self-contained unit with temperature, humidity, and pressure sensors as well as a GPS receiver. Weighing 15 g, it has a 120-minute battery life and a 16-megabyte storage capacity. The sampling rate is 1-3 Hz. The temperature sensor is of the bead thermistor type with a response time of 2 seconds. It has an accuracy of ± 0.3 °C and a resolution of 0.01 °C. The humidity sensor is the capacitive type with a 5 second response time. It has an accuracy of ± 5% relative humidity, and a resolution of 0.07% relative humidity. The sensor was mounted underneath the rotor arm of the Iris+ and placed near the body of the aircraft to minimize the effects of rotor downwash.

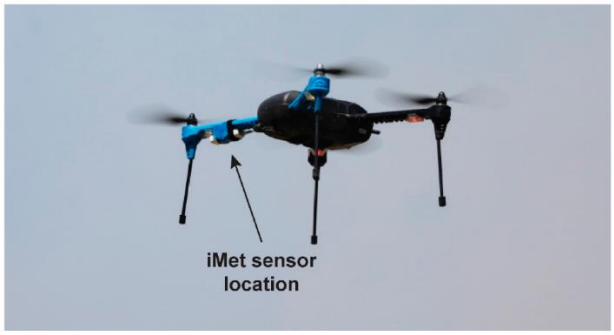

Figure 2.3. Location of iMet sensor placement on Iris+ sUAS platform.

Surface weather observations

Observations from nearby ground weather stations that are part of the Oklahoma Mesonet were used in the analysis to document meteorological conditions at the time of the sUAS flights and provide surface weather observations to supplement the sUAS-derived data. The Oklahoma Mesonet consists of 121 weather stations distributed across the state, with at least one station in

every county. The stations consist of a 10 m-tall tower with various sensors that measure more than 20 environmental variables including temperature, relative humidity, pressure, and wind speed (McPherson et al. 2007). The two Mesonet sites used in this analysis are the Marena site, which is located 11.3 km (7 miles) north of Coyle, OK (36° 3' 51" N, 97° 12' 45" W) and corresponds to the location of the June 29 data collection, and the Stillwater site, located 3.2 km (2 miles) west of Stillwater, OK (36° 7' 15" N, 97° 5' 42" W), which corresponds to the June 30 data collection event.

Methods

Sample Variograms

Variogram analysis was completed using the gstat package (Pebesma 2004) for the R statistical computing language. Only measurements from the ascent of each profile were used in the analysis since averaging data from both ascent and descent would skew variations due to a larger time difference, hence variation, from the measurements at lower altitudes. Also, it has been shown that the upon descent rotor downwash may introduce updrafts that would impact measurements due to the placement of the sensor on the aircraft (Jabob et al. 2017) As boundary-layer turbulence is inherently highly skewed, no observations were removed prior to analysis. For each dataset the initial lag distance was set to the average point spacing following Isaaks and Srivastava (1989); however, this resulted in a sparse sample variogram that did not fully represent the structure of the data. Lag distances were set to one-half the average point spacing and maximum lag distances were capped at one-half of the sampling area (maximum above ground altitude). However, these suggested parameterizations are based on terrestrial data, which does not exhibit the same scales of variability as atmospheric data.

The classical view of high Reynolds number (i.e., very turbulent) boundary layers, like the ABL, is that the turbulent flow field can be thought of as the superposition of eddies varying in size. The largest eddies would scale with the boundary layer thickness (~1 km) while the smallest are inversely related to the Reynolds number. Here, turbulent energy is supplied from the

largest scale motion, and that energy “cascades” down to smaller and smaller eddies until the eddies become sufficiently small that viscosity dissipates the turbulent energy.

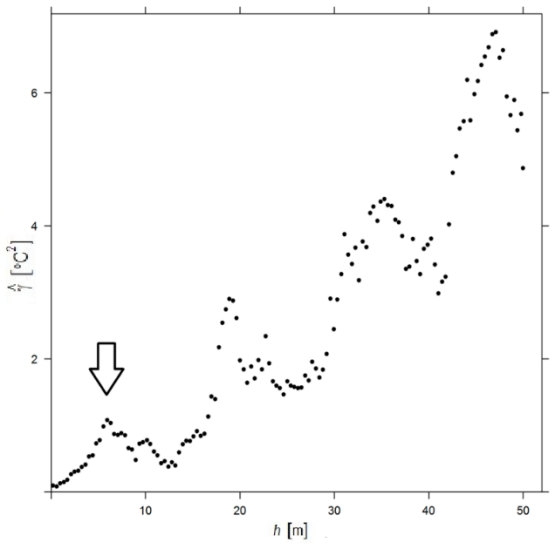

Figure 2.4. Sample variogram displaying increasing scales of variability (scale domains) with distance.

Variograms carry information about all of these scales. In fact, the autocorrelation is commonly used to determine the largest turbulent scales (integral scale) as well as the Taylor microscale. The integral scale is determined from integration of the autocorrelation, and the Taylor microscale (an intermediate length scale at which turbulent motions are significantly impacted by viscosity) is related to the shape of the autocorrelation near zero lag. Since variograms are a modified form of an autocorrelation, they carry information about these turbulent structures (Pope 2000). Given this information, there is expected to be a certain degree of spatial autocorrelation for all atmospheric samples within the ABL (i.e., no plateau is expected in the variogram until outside of the ABL, which could be on the order of 1 km). Thus, instead of a single plateau indicating the range of spatial autocorrelation as is typical for terrestrial measurements, the absolute semivariance will exhibit multiple peaks corresponding to the various scales of dominant turbulent structures within the ABL. Since the objective of this research is to

identify the finest spatial scale needed to capture the structure of atmospheric measurements in vertical profiles, the goal is to identify the separation distance where the semivariance first peaks, which is expected to correspond to the finest scale domain, and use this as the maximum lag distance for variogram modeling (Figure 2.4). Other studies have noted similar structures in vertical samples of geological measurements and refer to this phenomenon as the hole or periodicity effect (Isaaks and Srivastava 1989).

Fitting Model Variograms

Noise and limited sample size can result in some fluctuations within the semivariance estimates, even within each scale domain. Consequently, the data are typically modeled to mitigate the influence of scatter in the variogram and accurately identify the range, sill, and nugget. There are many commonly used model variograms including Gaussian, spherical, and exponential; and proper model selection depends on the spatial continuity of the variable. The chosen model variogram is often eventually used to select ideal weights for further geostatistical analyses, such as kriging, and selecting an incorrect model at this stage can adversely affect the accuracy of subsequent estimates.

Most often, visual inspection is performed on the sample variogram to select the most appropriate model. The sample variograms most closely matched a Gaussian variogram model, and Gaussian models typically work well when there is a small nugget and the curve appears smooth (Burrough et al. 2015). Following visual assessment, Gaussian model variograms were fit to all sample variograms. The Gaussian model is defined as

$$\gamma(h) = 1 - exp\left(-\left(\frac{a}{h}\right)^2\right) \tag{2.5}$$

here h is the lag and a is the sill. Models were fit in gstat by minimizing least squares.

Obukhov Length Scale Calculations

The Obukhov length scale

$$L = \frac{-\rho C_p T u_\tau^3}{\kappa g H} \tag{2.6}$$

is widely used within micrometeorology to characterize the ABL. It represents a nominal height at which the turbulent production from wind shear is comparable to that from buoyancy. Here, ρ is the density of air at temperature *T*, *Cp* is the specific heat capacity at constant pressure, $u\tau$ is the friction velocity, κ is the von Kármán constant, and *H* is the sensible heat flux. Like most ABL measurements, the current study lacks accurate measurements of $u\tau$ and *H*. However, this work follows the approach of Dyer (1974) and Essa (1999) to estimate *L* given nearby measurements of the surface gradients of wind speed and temperature. Measurements from either the Marena (June 29, 2016) or Stillwater (June 30, 2016) Mesonet sites are used to measure temperature (1.5 and 9 m above ground), wind speed (2 and 9 m above ground), and local pressure. These measurements are used to determine potential temperatures (θ_1 *and* θ_2), potential temperature difference ($\Delta\theta$), and wind speed differences ($\Delta u = u_2 - u_1$), which are then used to estimate the Richardson number

$$R_i = \frac{g \Delta z \Delta \theta}{\theta_1 \Delta u^2} \tag{2.7}$$

where *g* is gravitational acceleration and Δz is the difference in heights where measurements are acquired. Then, following Businger et al. (1971)

$$\zeta = \frac{\phi_m^2}{\phi_h} R_i \tag{2.8}$$

where $\zeta = z/L$, *z* is the geometric mean height of the measurements used in R_i, ϕ_m is an assumed universal function for momentum, and ϕ_h is an assumed universal function for heat exchange. The universality of these functions is debated, but for the current work they are estimated using constants from Dyer (1974),

$$\phi_m = \begin{cases} (1 - 16\zeta)^{-0.25} & \zeta < 0 \\ (1 + 5\zeta) & \zeta > 0 \end{cases} \tag{2.9}$$

$$\phi_h = \begin{cases} (1 - 16\zeta)^{-0.5} & \zeta < 0 \\ (1 + 5\zeta) & \zeta > 0 \end{cases}$$

allowing for an iterative process to solve for ζ, which provides an estimate for *L*. The functional forms of the universal function as well as the constant values are questionable, but even under ideal conditions its accuracy within the Obukhov similarity theory is only 10%–20% (Essa 1999).

Results

Flight Summaries

Summary statistics for the 12 flights show similar flight conditions within and between the two flight dates (Table 2.1). Flights occurred during early morning (pre-sunrise) and late morning/mid-afternoon to capture temperature inversions from radiative heating during the early part of the day. Each flight lasted between 3 and 5 minutes and reached maximum above ground level (AGL) altitudes between 100 and 120 m. On average, 240 measurements were collected for each variable during each flight. Ascents averaged speeds of 1.96 m/s resulting in an average point spacing of 0.55 per m. Mean temperatures ranged from 21.0°C to 30.6°C and mean relative humidity (RH) measurements ranged from 54.7% to 64.3%.

Flight ID	Date	Start Time	End Time	Max Alt. AGL (m)	No. Obs.	Min Temp	Mean Temp	Max Temp	Min RH	Mean RH	Max RH
A1	29-Jun	5:47:30	5:52:06	107.87	277	18.11	21.02	24.94	46.6	62.98	76.1
A2	29-Jun	6:26:06	6:29:41	110.95	216	19.06	22.13	26.47	41.0	58.8	70.6
A3	29-Jun	9:23:45	9:27:23	111.21	219	23.77	24.58	26.33	51.3	57.85	67.1
A4	29-Jun	12:05:23	12:09:55	111.39	273	27.51	28.92	33.39	47.6	55.28	59.9
A5	29-Jun	13:30:48	13:37:42	111.97	415	29.35	30.6	36.09	47.7	54.71	60.5
B1	30-Jun	6:02:10	6:05:56	130.06	227	21.09	23.46	25.07	54.9	64.26	76.3
B2	30-Jun	6:18:54	6:22:22	130.48	210	21.27	23.71	25.17	54.5	62.74	74.5
B3	30-Jun	6:34:31	6:37:59	133.30	213	21.75	23.6	24.84	56	63.01	72.6
B4	30-Jun	6:52:45	6:56:05	135.40	202	22.13	23.55	24.63	56.6	62.32	69
B5	30-Jun	7:33:31	7:38:06	132.44	278	22.64	23.52	24.55	58	63.98	68.9
B6	30-Jun	8:41:57	8:44:32	137.10	156	25.02	25.61	26.19	55.2	57.15	59.4
B7	30-Jun	9:06:49	9:10:00	141.99	193	25.39	26.05	28.17	49.6	55.08	57.3

Table 2.1. Flight information and summary statistics. Temperature (Temp) is reported in degrees Celsius and relative humidity (RH) is reported in percent. Start times are at the beginning of each ascent and end times are the time at which the flight reached maximum altitude. All times are local (UTC-5).

Plots of potential temperature and RH for each flight show the profile inversions over the course of each day (Figure 2.5). Data have been grouped into bins for display purposes, with bin

sizes determined by dividing the range of altitude measurements for each flight into deciles. Mean temperature and RH values for each bin were differenced from the overall mean and plotted against the mean altitude of each bin. Standard deviations for each bin are plotted as error bars.

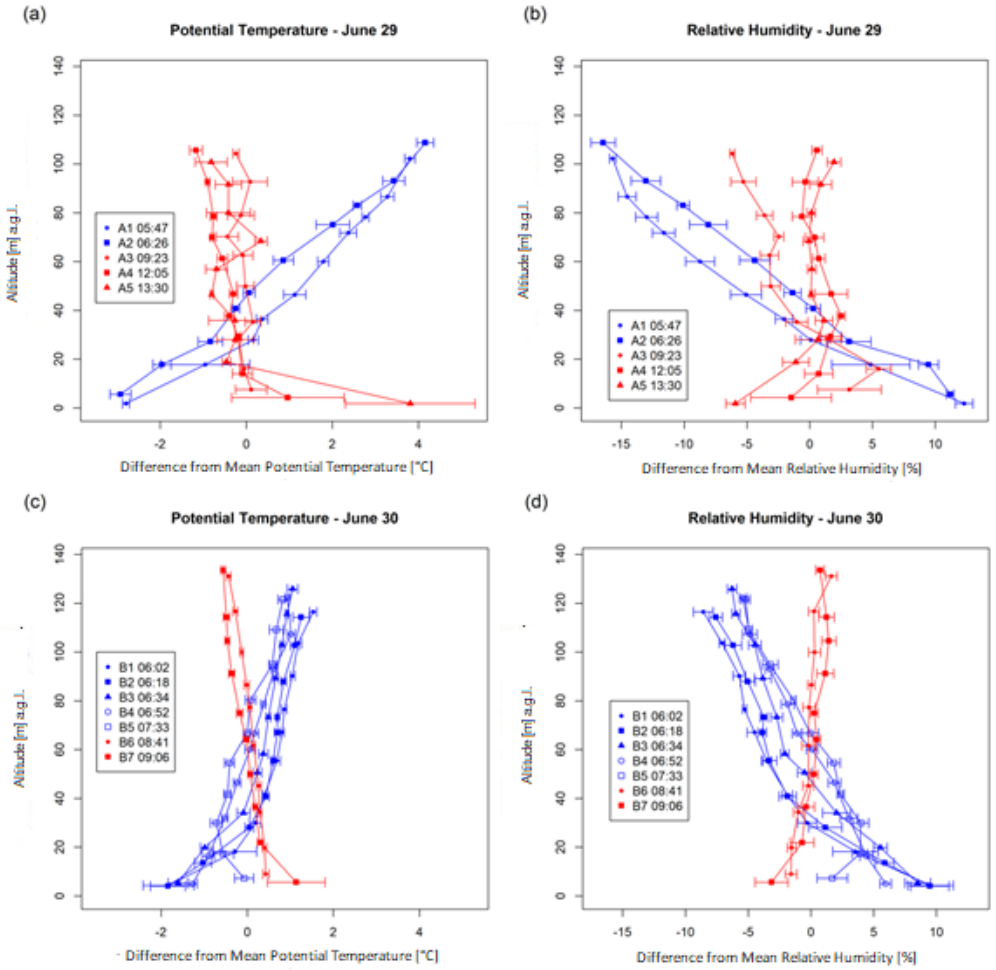

Figure 2.5. Profile plots for (a) June 29 potential temperature, (b) June 29 relative humidity, (c) June 30 potential temperature, and (d) June 30 relative humidity. Flight start times are in Central Daylight Time (UTC-5).

The two earliest flights on June 29 (A1 and A2) show gradually increasing potential temperature and decreasing RH as altitude increases (blue plots in Figure 2.5a and 2.5b). For the later flights (red plots), potential temperature and RH are more homogenous across altitude with slight inversions occurring for RH between the surface and 40 m. For the later flights, both

variables exhibit relative stability above 40 m, indicative of a classic stable boundary layer (Stull 1988). The homogeneity in temperature and RH above 40 m results from the atmospheric mixing that occurs as the sun warms the earth and heat begins to radiate upward. The same general trends were observed the following day with flights occurring prior to 08:00 showing an increasing (Temp) or decreasing (RH) relationship with altitude, while flights occurring after 08:00 show less variability and do not show any inversions (Figures 2.4c and 2.4d). Overall, there was greater variability in the observations captured on June 29 compared to June 30 both in terms of the overall spread of measurements in the profile as well as the standard deviations for each bin.

Variogram modeling

Semivariances were computed for each pair of samples satisfying the maximum separation distance, and Gaussian models were fit to the sample points. Two examples (Figure 2.6) illustrate how the Gaussian model plateaus at the range distance where the sample measurements are no longer spatially autocorrelated within the first scale domain (as determined by the maximum separation distance). The temperature data (Figure 2.7a) show the nugget being located at approximately 0.015 on the semivariance (y) axis, the sill being located at approximately 0.09, and the range being located at approximately 6 m on the distance (x) axis. The RH data for the same flight show a similar structure, but the semivariance values for the nugget and sill are much higher while the lag distance for the range is only about 3 m. Despite their differences, it is clear from these plots where the semivariance plateaus or levels off, indicating the range distance at which the spatially autocorrelated structure of the data can be captured: within distances of 3.4 m and 1.8 m for temperature and RH, respectively.

The variogram models for the remaining flights exhibited similar spatial structures to those in Figure 2.6 but with varying values for nuggets, sills, and ranges. In general, nugget values did not vary much between the two days for either temperature or RH. Nugget values ranged from 0.002 to 0.101 for temperature and were slightly higher for RH, ranging from 0.111 to 1.402. Small nugget values indicate that at very small sampling lag distances (0.5 m), there is not much

variation between measurements. Large nugget values are common for terrestrial, geographic phenomena (e.g., geology), where there can be large differences in a measured variable such as mineral content at small distances (e.g., gold nuggets). Large nuggets (> ½ the sill) are not expected when capturing atmospheric data and were not observed during this sampling campaign.

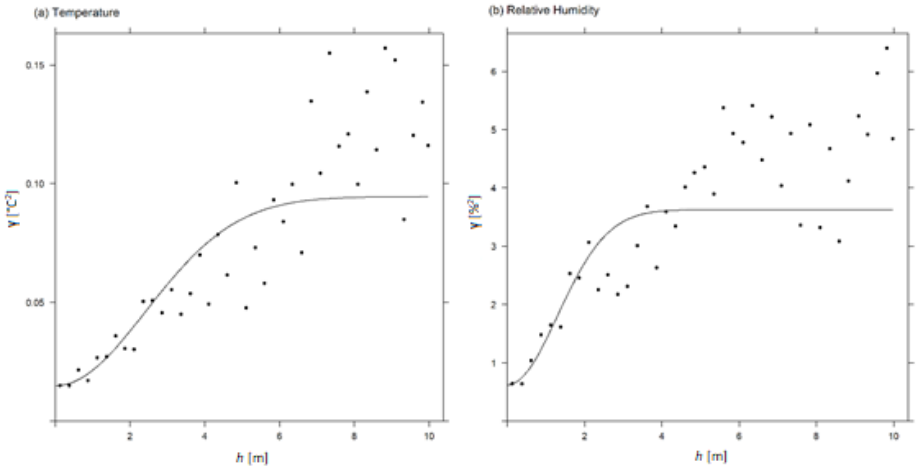

Figure 2.6. Sample variograms with Gaussian variogram models fit to (a) temperature and (b) relative humidity data from flight A3 on June 29.

Sill values for temperature also showed little variability across both days, ranging between 0.095 and 1.214 on June 29 and between 0.020 and 0.518 on June 30. Sill values for RH were more variable, ranging from 3.627 to 12.594 on June 29 and from 0.248 to 3.920 on June 30. For both temperature and RH, there was greater variation in sill position for the June 29 flights compared to the June 30 flights. The sill value quantifies the maximum semivariance at the range distance identified by the variogram model (see Figure 2.4). Larger sill values indicate larger variances between samples at the distance where spatial autocorrelation begins to plateau. In general, sills were larger for both variables on both days for the early morning flights compared to the later flights because the atmosphere had not mixed at that point, so there is greater variance in measurements between lag distances.

Flight ID	Temp Sill	Temp Range	Temp Nugget	Temp RMSE	RH Sill	RH Range	RH Nugget	RH RMSE	*L*(m)
A1	1.123	5.741	0.093	0.227	9.930	4.825	1.153	1.339	69
A2	0.685	10.234	0.023	0.034	12.502	8.357	0.510	2.071	1189
A3	0.094	3.356	0.015	0.019	3.170	1.482	0.571	1.026	-3719
A4	1.872	3.457	0.104	1.230	9.648	1.913	1.464	5.526	-4271
A5	-	-	-	-	1.607	0.403	1.277	0.790	-4472
B1	0.497	5.317	0.003	0.054	4.634	5.058	0.180	0.463	4477
B2	0.225	6.474	0.012	0.063	3.996	6.388	0.427	0.853	5585
B3	0.192	14.863	0.003	0.015	1.292	4.898	0.110	0.192	4123
B4	0.047	8.433	0.003	0.006	0.489	2.919	0.173	0.130	10944
B5	0.157	12.356	0.010	0.011	0.588	2.756	0.183	0.069	-25565
B6	0.031	24.425	0.002	0.001	0.502	14.177	0.207	0.043	-7928
B7	0.066	7.655	0.002	0.019	0.556	2.169	0.118	0.072	-5409

*Variogram model could not be fit to temperature measurements from flight A5.

Table 2.2. Variogram results and fit diagnostics (RMSE) for all flights showing sill, range, and nugget values for temperature (Temp) and relative humidity (RH).

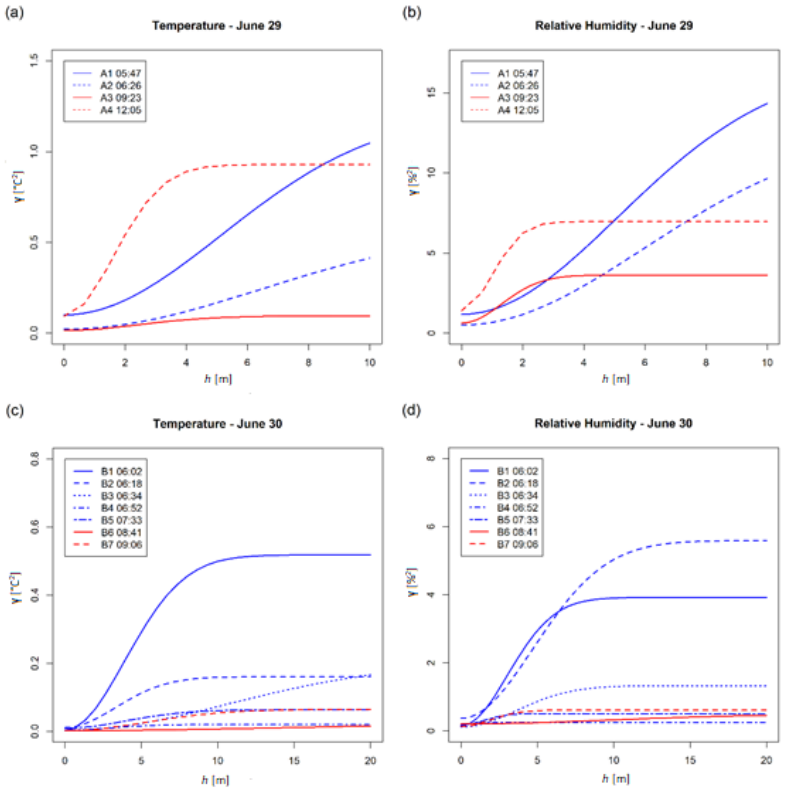

Figure 2.7. Fitted Gaussian variogram models for (a) June 29 temperature, (b) June 29 relative humidity, (c) June 30 temperature, and (d) June 30 relative humidity.

It should be noted that the sills for RH on June 29 were several times larger than those captured on June 30. These differences may be due to the more variable weather conditions on June 30 as observed from the Mesonet towers (Figure 2.8). In particular, wind speeds were

greater on the morning of June 30 indicating increased frictional mixing within the lower portion of the boundary layer (100–150 m). As seen in the profile plots (Figure 2.5), on June 29 the range of RH values is much greater compared to June 30, and the maximum altitude of the June 29 flights is about 20–30 m less than those on June 30 (Table 2.1). Together, these results indicate the atmosphere was likely less mixed, and therefore more variable, during the morning flights on June 29 compared to June 30. As a result, the RH measurements at each distance lag were more dissimilar on June 29 than they were on June 30, manifesting in greater sill values.

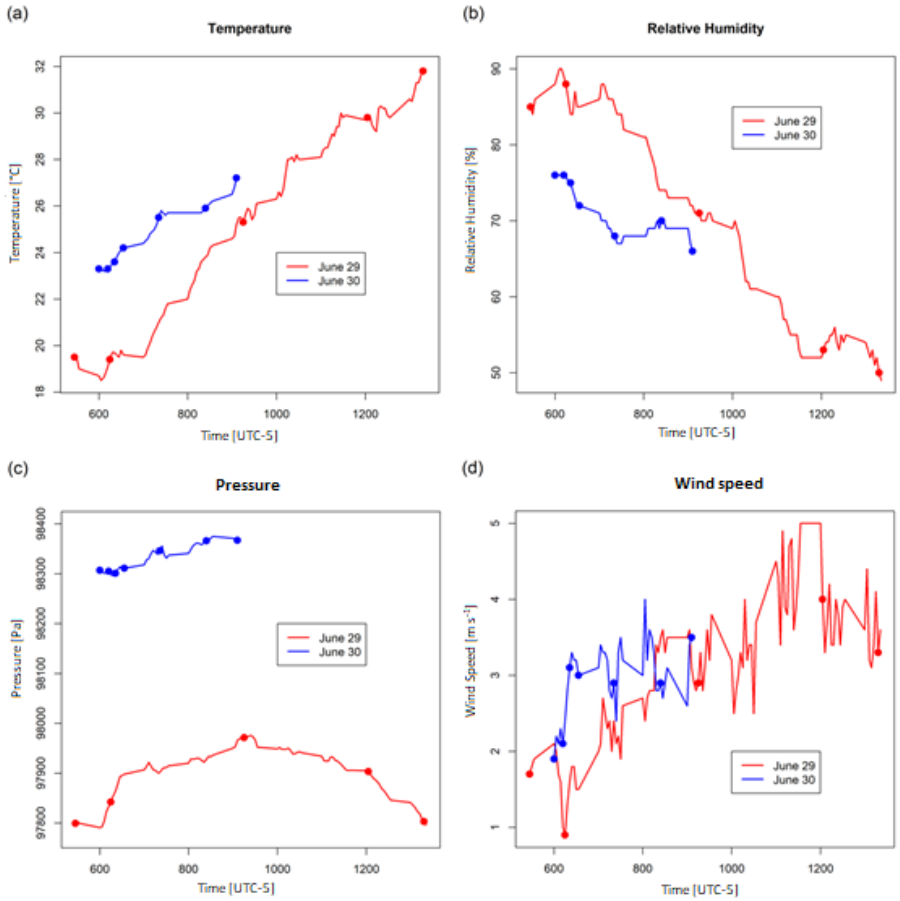

Figure 2.8. Weather conditions at corresponding Mesonet stations for (a) temperature, (b) relative humidity, (c) pressure, and (d) wind speed. Dots indicate start time of each ascent.

Range values show several interesting trends. On June 29, the ranges for temperature and RH are quite similar across each flight, with larger ranges computed for the early morning flights and comparably smaller ranges for the later flights. For the June 30 flights, with the exception of Flight B6, and an outlying value for temperature during Flight B3, range values were relatively

stable, ranging from about 2–5 m. These results indicate that during the early morning when the lower atmosphere is not yet mixed, samples can be collected at larger lag distances while still capturing the spatial structure of the profile. Meanwhile, when the atmosphere is mixed, particularly during latter times of the day, more frequent sampling is needed to capture changes in the vertical profile. These findings are consistent with the expectation that the ABL is at a lower Reynolds number in the morning when it is forming, which results in the finest scales being larger (i.e., smallest turbulent length scales are inversely related to Reynolds number). Thus, fewer measurements spaced further apart are needed to capture the structure of the atmosphere before the earth's surface warms and mixing occurs.

Standardized variograms allow for comparison of range values irrespective of the varying sill values, which can aid in interpretation. Variograms were standardized to a semivariance of 1 by plotting the semivariance minus the nugget divided by the partial sill (sill-nugget) against the separation distance (Figure 2.9). For the June 29 flights, there is a clear distinction between the early morning (red lines) and late morning/early afternoon flights (blue lines). Range values in the late morning are smaller than those in the early morning, again suggesting that more frequent sampling is needed to capture the atmospheric profile prior to mixing. On June 30, where there was less change in the atmosphere between the early morning and late morning/early afternoon flights, there is less distinction in range values. Values were relatively stable across all flights, although range values decreased slightly as the morning progressed. Flights B3 and B6 also appear as outliers, particularly in the temperature plot (Figure 2.9c).

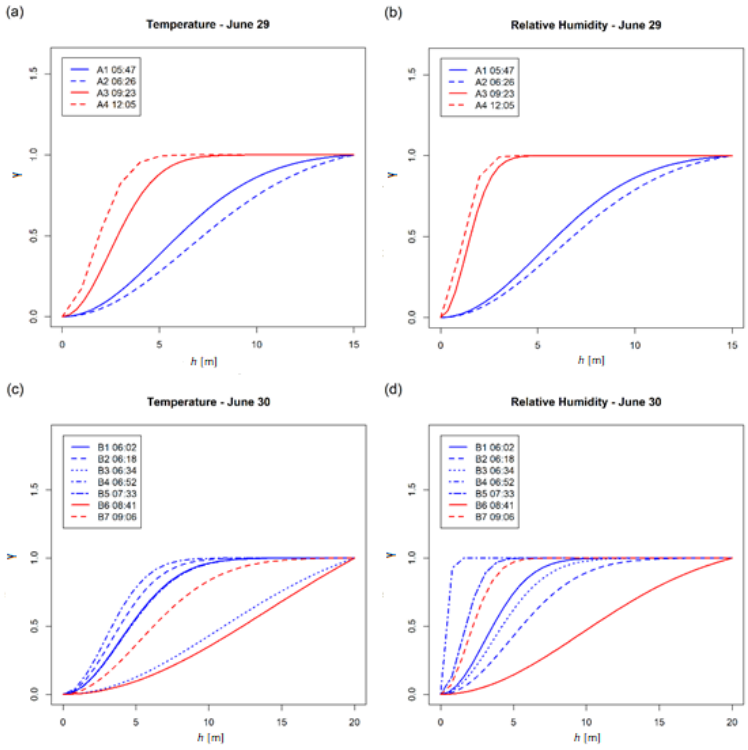

Figure 2.9. Standardized variogram models for (a) June 29 temperature, (b) June 29 relative humidity, (c) June 30 temperature, and (d) June 30 relative humidity.

Discussion

While turbulent flow fields such as an ABL obey governing equations, their signals are not repeatable, which forces the results to be reported as statistics for comparison. Autocorrelations provide fundamental insights about the size and distribution of coherent structures within a turbulent flow (e.g., Yeung et al. 2002, Elbing et al. 2010, Horn et al. 2015). Variograms generated for atmospheric measurements in the ABL capture the distribution of scales via multiple peaks or plateaus at which autocorrelation dissipates over a range of length scales, with the smallest structures having the highest correlation (i.e., smallest semivariance). Thus, the largest sample separation distance that can still capture the smallest scale structures should be related to the range observed for the first peak/plateau from the semivariance plot (see Figure 2.4). Following this assumption, it was found that optimal sampling scales for vertical measurements of temperature taken from sUAS were about 5 m for early morning flights prior to

atmospheric mixing. Once mixing had occurred, more frequent sampling was needed (~3 m) to capture the data structure. The optimal sampling scales for RH were slightly smaller than those for temperature with range values of approximately 1.5–2 m after mixing had occurred. Again, these scales were found to be sufficient for capturing the first scale domain for temperature and RH within the lower portion of the ABL for this study, but further research is needed to identify the periodicity of additional scale domains within the ABL. Additionally, researchers looking to capture micro fluctuations may require smaller sampling scales.

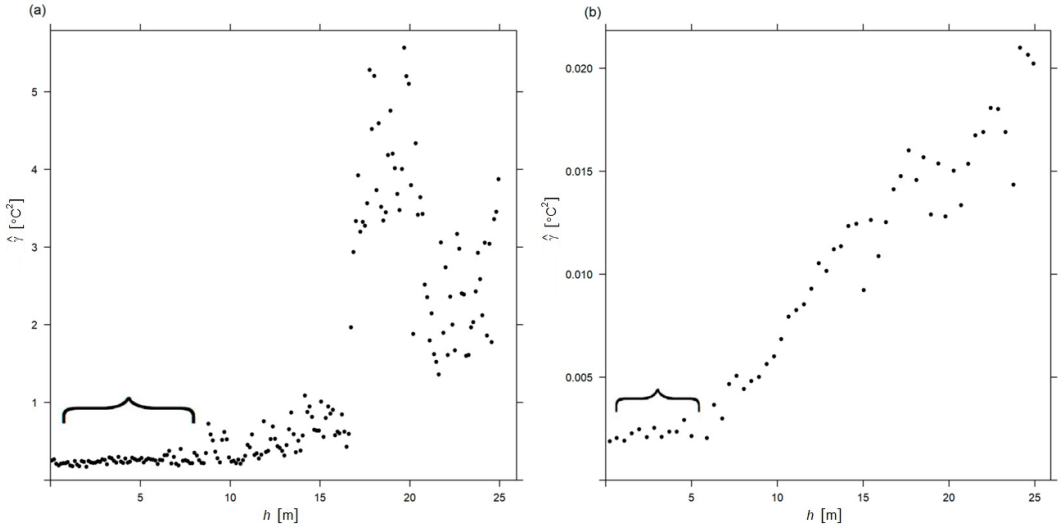

Figure 2.10. Sample variograms of (a) Flight A5 on June 29 and (b) B6 on June 30.

Flight A5 could not be modeled with a semivariogram, and therefore results were not reported or included in our analysis. The likely reason that A5 could not be modeled is because as the process of boundary-layer mixing unfolds, the portion of the atmosphere in direct contact with the earth becomes homogenized (Figure 2.10a). With homogenization, the first scale domain becomes smaller and smaller and eventually is undetectable in the sample variogram. This phenomenon is known as the pure nugget effect and makes model fitting difficult because there is no identifiable plateau within the maximum lag distance. While the absence of plateau within the maximum lag distance signals that the first scale domain is located at a larger scale, it does not change the minimum sampling scales that should be used when knowledge about the structure of

the atmosphere is unknown. For Flight B6, which exhibited a similar pattern (Figure 2.10b), even though a variogram could be fit to the data, the associated range distances for temperature (19.934 m) and RH (13.597 m) are likely more representative of the second scale domain.

Conclusion

This study used variogram modeling, a common geostatistical technique in the geographical sciences, to determine the optimal vertical sampling scales for two atmospheric variables (temperature and relative humidity) captured from a small, unmanned aircraft system (sUAS). The key findings from our analysis show that variogram modeling can serve as a useful methodology for identifying the finest scale domain of atmospheric vertical profiles. Future work will focus on capturing the entire extent of the ABL as well as integrating optimal spatial sampling scales in the horizontal direction with those in the vertical dimension as a basis for collecting measurements from sUAS.

References

Bendix, J., Fries, A., Zárate, J., Trachte, K., Rollenbeck, R., Pucha-Cofrep, F., ... & Naranjo, C. (2017). RadarNet-Sur first weather radar network in tropical high mountains. *Bulletin of the American Meteorological Society*, *98*(6), 1235–1254.

Bolstad, P. (2012). *GIS Fundamentals: A First Text on Geographic Information Systems*, 4th ed: Eider Press, White Bear Lake, MN.

Burrough, P.A., McDonnell, R., McDonnell, R.A., Lloyd, C.D. (2015). *Principles of Geographical Information Systems*, 3rd ed; Oxford University Press: New York.

Businger, J.A., Wyngaard, J.C., Izumi, Y., & Bradley, E.F. (1971). Flux-profile relationships in the atmospheric surface layer. *Journal of the atmospheric Sciences*, *28*(2), 181–189.

Cassano, J.J. (2014). Observations of atmospheric boundary layer temperature profiles with a small unmanned aerial vehicle. *Antarctic Science*, *26*(2), 205–213.

Chowdhury, A.R., Sheldon, D., Maji, S., Learned-Miller, E. Distinguishing weather phenomena from bird migration patterns in radar imagery." *In Proceedings of the IEEE Conference on Computer Vision and Pattern Recognition Workshops*, 2016, 10–17.

Crick, C., & Pfeffer, A. (2012). Loopy belief propagation as a basis for communication in sensor networks. *arXiv preprint arXiv:*1212.2465.

Doviak, R.J.; Zmic, D.S. (1993). Doppler Radar and Weather Observations, 2nd ed: Academic Press, San Diego.

Dyer, A. (1974). A review of flux-profile relationships. *Boundary-Layer Meteorology*, *7*(3), 363–372.

Elbing, B R., Winkel, E.S., Ceccio, S.L., Perlin, M., & Dowling, D.R. (2010). High-reynolds-number turbulent-boundary-layer wall-pressure fluctuations with dilute polymer solutions. *Physics of Fluids*, *22*(8), 085104.

Elston, J., Argrow, B., Stachura, M., Weibel, D., Lawrence, D., & Pope, D. (2015). Overview of small fixed-wing unmanned aircraft for meteorological sampling. *Journal of Atmospheric and Oceanic Technology*, *32*(1), 97–115.

Essa, K.S. Estimation of Monin-Obukhov Length Using Richardson and Bulk Richardson Number. *In Proceedings of the 2nd Conference on Nuclear and Particle Physics*, Cairo, Egypt, 13–17 November 1999.

Farnsworth, A., Van Doren, B.M., Hochachka, W.M., Sheldon, D., Winner, K., Irvine, J., Geevarghese, J. Kelling, S. (2016). A characterization of autumn nocturnal migration detected by weather surveillance radars in the northeastern USA. *Ecological Applications*, *26* (3), 752–770.

Frazier, A.E., Mathews, A.J., Hemingway, B.L., Crick, C., Martin, E., & Smith, S.W. Integrating small Unmanned Air-Craft Systems (sUAS) into Meteorology and Atmospheric Science: Challenges and Opportunities for GIScience. *GI_Forum 2017*, 5, 189-199.

Frew, E.W., Elston, J., Argrow, B., Houston, A., and Rasmussen, E., (2012). Sampling severe local storms and related phenomena: using unmanned aircraft systems. *IEEE Robotics & Automation Magazine*, *19*(1), 85–95.

Fujita, T.T. *A review of researches on analytical mesometeorology. Mesometeorology Project*, Department of the Geophysical Sciences, University of Chicago. 1962.

Golbon-Haghighi, M.H., Zhang, G., Li, Y., Doviak, R.J. (2016). Detection of ground clutter from weather radar using a duel-polarization and duel-scan method. *Atmosphere*, 7, 83.

Horn, G.L., Ouwersloot, H.G., De Arellano, J. V.G., & Sikma, M. (2015). Cloud shading effects on characteristic boundary-layer length scales. *Boundary-Layer Meteorology*, *157*(2), 237–263.

Houston, A.L.; Argrow, B.; Elston, J.; Lahowetz, J.; Frew, E.W.; Kennedy, P.C., (2012). The collaborative Colorado–Nebraska unmanned aircraft system experiment. *Bull. Am. Meteorol. Soc.*, *93*(1), 39–54.

Isaaks, E.H.; Srivastava, R.M. (1989). *Applied Geostatistics.* Oxford: Oxford University Press.

Jacob, J.D., Axisa, D. and Oncley, S., (2017). Unmanned aerial systems for atmospheric research: instrumentation issues for atmospheric measurements. *In Proceedings of the NCAR/EOL Community Workshop for Unmanned Aerial Systems for Atmospheric Research, Boulder, CO, USA*, 21–24.

Jensen, J.R. (2015). *Introductory digital image processing: A remote sensing perspective*, 4th ed: Upper Saddle River, NJ: Pearson Prentice Hall.

Konrad T., Hill M., Rowland R., Meyer J. (1970). A small, radio-controlled aircraft as a platform for meteorological sensors. *Johns Hopkins APL Tech Dig* 10, 11–19.

LaDue, D.S., Heinselman, P.L., Newman, J.F. (2010). Strengths and limitations of current radar systems for two stakeholder groups in the southern plains. Bull. Amer. Meteor. Soc. 2010, 7, 899–910.

Mayer, S., Sandvik, A., Jonassen, M. O., Reuder, J., (2012). Atmospheric profiling with the UAS SUMO: A new perspective for the evaluation of fine-scale atmospheric models. *Meteorol. Atmos. Phys*. 116, 15–26.

McPherson, R.A., Fiebrich, C.A., Crawford, K. C., Kilby, J.R., Grimsley, D.L., Martinez, J.E., Basara, J.B., Illston, B.G., Morris, D.A., Kloesel, K.A. (2007). Statewide monitoring of the mesoscale environment: a technical update on the Oklahoma Mesonet. *J. Atmos. Ocean. Tech*. 24, 301–321.

Oliver, M.A., Webster, R. (2015). *Basic steps in geostatistics: The variogram and k*riging, 1st ed; Cham, Switzerland: Springer.

Pebesma, E.J., (2004). Multivariable geostatistics in S: the gstat package. *Computers & Geosciences*, *30*(7), 683–691.

Pope, S. (2000). *Turbulent flows*. New York: Cambridge University Press

Roadman, J., Elston, J., Argrow, B., & Frew, E. (2012). Mission performance of the tempest unmanned aircraft system in supercell storms. *Journal of Aircraft*, *49*(6), 1821-1830.

Stull, R.B. (1988). *An introduction to boundary layer meteorology*. Dordrecht: Kluwer Academic Publishers.

Yeung, P. (2002). Lagrangian investigations of turbulence. *Annual Review of Fluid Mechanics*, *34*(1): 115-142.

CHAPTER III

HIGH RESOLUTION ESTIMATION AND SPATIAL INTERPOLATION OF TEMPERATURE STRUCTURE IN THE ATMOSPHERIC BOUNDARY LAYER USING A SMALL UNMANNED AIRCRAFT SYSTEM

Introduction

Small-scale fluctuations in temperature are of considerable importance in meteorology. Practically, their effects on sound and light propagation in the atmosphere allow for their use in calibration of remote sensing instruments (Wainwright et al. 2015). Theoretically, the small-scale turbulent motions that cause these fluctuations are most likely to be universal, leading to a better understanding of turbulence at all scales (Sreenivasan and Antonia 1997). Small-scale fluctuations of temperature have been theorized to be analogous to fluctuations of velocity, which led Obukhov (1949) to characterize small-scale temperature fluctuations in the context of Kolmogorov similarity theory. Kolmogorov (1941a) proposed that in the inertial range, where the statistics of the flow are dependent only on the energy dissipation rate, eddies contained therein are homogenous (spatially stationary), isotropic, and independent of the larger, energy-containing eddies.

In accordance with Kolmogorov's theory, in the inertial range, temperature increments represented by $T(x+h) - T(x) = \Delta T$, where T is the temperature measured at location x, and h is a spatial separation distance, should scale as

$$\langle \Delta T(h)^p \rangle = C_p h^{\frac{p}{3}}, \tag{3.1}$$

where p is the moment of temperature increments, and C_p is a proportionality factor. When $p = 2$,

the square of the temperature increments, $\Delta T(h)^2$, is the second-order structure function, and C_2 is known in micrometeorology as the temperature structure function parameter or more commonly the temperature structure parameter, C_T^2. The value of p in Equation 3.1 need not be an integer (Mathieu and Scott 2000), and evidence suggests that flows in the atmospheric boundary layer (ABL) deviate from this scaling relationship, a phenomenon known as intermittency (Monin and Yaglom 1975). Kolmogorov (1941a) proposed that the energy dissipation rate remains constant, leading to a linear similarity relationship between the scaling exponent $p/3$ and the structure function of order p. However, the large energy-containing eddies, which provide the statistical input to the small-scale energy cascade, are thought to vary in intensity, causing random fluctuations in temperature and velocity increments to propagate down through the energy cascade (Mathieu and Scott 2000). This propagation leads to a breakdown of the theorized similarity relationship, particularly at higher-order moments. It has been suggested that the structure function of temperature is more sensitive to intermittency than the structure function of velocity (Antonia et al. 1984), although Gawedski and Kupainien (1995) demonstrated that the scaling relationships in Equation 3.1 hold when $p = 2$ for temperature measurements.

The structure functions and inertial range scaling relationships of temperature have been studied empirically in both the laboratory environment (Cioni et al. 1995) as well as in the ABL (Vindel et al. 2008). However, most data collection occurs in the time domain, and measurements are converted to the spatial dimension through the application of Taylor's (1938) frozen turbulence hypothesis, which is a key assumption in assessing the validity of the scaling relationships (Grossman and Lohse 1994). Capturing a spatial snapshot of conditions in the ABL has remained challenging. Recent technological advancements have led to the adoption of small unmanned aircraft systems (sUAS) in the atmospheric sciences, as they provide the capability for collecting data to compute inherently spatial, two-point correlation statistics (Jacob et al. 2018).

The use of sUAS for atmospheric sampling is not entirely new, however, and goes back to at least the 1960s (Smith 2011). Konrad et al. (1970) proposed using small, remotely controlled

aircraft for collecting temperature and humidity data near the ground. More recent advancements in sUAS technology have led to their use in a variety of meteorological sensing applications, such as high-resolution distributed temperature sensing of the morning ABL transition (Higgins et al. 2018) and pre-convective environments (Koch et al. 2018), obtaining profiles of vertical wind velocity for cloud-aerosol interactions (Calmer et al. 2018), and estimating sensible heat flux (Lee et al. 2017). A handful of studies have estimated the temperature structure function (and correspondingly C_2) using sUAS in the ABL (van den Kroonenberg et al. 2012; Bonin et al. 2015; Wainwright et al. 2015; Braam et al. 2016; Platis et al. 2017) and were able to resolve the inertial range through the theorized scaling relationship (Equation 3.1). However, these studies compiled estimates of C_2 collected at discrete altitudes using horizontal transects across heterogeneous terrain (van den Kroonenberg et al. 2012) or spiral ascents, estimating C_2 horizontally at discrete attitudes and constructing a C_2 profile (e.g., Bonin et al. 2015; Wainwright et al. 2015). Horizontal estimates of temperature structure may be subject to influences of surface heterogeneity, making it difficult to distinguish the surface influences on the statistics of the turbulence (van den Kroonenberg et al. 2012; Platis et al. 2017). C_2 has been estimated from continuous vertical sUAS profiles by Platis et al. (2016).

The question becomes whether estimation of C_2 from continuous profiles is necessary and appropriate. Isotropic turbulence, within which C_2 estimates are valid, is inherently three-dimensional. For example, it has been suggested that coherent structures in the ABL are oriented obliquely at angles up to 45 degrees from the surface (Marusic and Heuer 2007). Additionally, the impacts of shear and buoyancy on the transport of heat and momentum in the ABL are predominately observed in the vertical direction. Practically speaking, the structure function is the key component to the spatial interpolation methodology known as kriging (or Gaussian process regression). Most natural phenomena, such as temperature, exhibit some degree of spatial autocorrelation, that is, measured values nearer to each other are more similar to each other than those measured at greater distances. The structure function (or variogram) is a measure of spatial

autocorrelation. For these reasons, estimating C_2 from continuous vertical profiles has value not only for understanding the physical process, but also for representing it statistically.

Given the need for investigating temperature structure using vertical profiles, there are challenges to overcome. First-order differences may be stationary at short separation distances; however, the structure function estimated data spanning greater vertical separation distances are, by nature, spatially nonstationary, and thus a modified form of the structure function must be used to account for the non-constant mean across the vertical spatial domain. Geostatistics is a branch of spatial statistics focusing on predicting probability distributions of spatial and spatiotemporal datasets. Geostatistics is widely used in the earth sciences, including geography and geology, to predict values of parameters between sampled data points. Geostatistical approaches are well suited for random variables due to the ability to accommodate the spatial nonstationarity and spatial dependence inherent to such data. Kolmogorov (1941b) proposed the structure function to assign weights for optimal prediction of turbulent quantities. Conceptually similar techniques were simultaneously developed by others in a variety of disciplines (see Cressie 1990 for a thorough history), but the theory of geostatistics was coalesced by Matheron (1963). This theoretical foundation serves as the basis for using geostatistical analysis for atmospheric research, which underpins this study.

The objective of this research is to characterize the spatial structure of vertical temperature observations through profiles captured via sUAS using geostatistical tools. To this end, three sub-objectives were pursued:

1. Capture the structure of the temperature field in the vertical dimension using the variogram to identify sample separation distances that are inherent to the inertial subrange of turbulence by assessing ranges of separation distances that follow a 2/3 power law model.

2. Assess the degree of deviation from the theorized second-order scaling relationships through cross validation of universal kriging, a distance-weighted method of interpolation that will use the 2/3 power law model for assignment of weights.
3. Determine specific portions of the continuous, vertical profile for which the 2/3 power law model best fits the data through assessment of prediction residuals at each estimated point.

Theory

For a continuous variable such as temperature, at any given point, x, there is not a single value, but one of any number of potential temperature values. The realization of a single value is a random variable $Z(x)$, having a mean, standard deviation, and probability density function. A random variable for all locations in $x = (x_1, x_2 \ldots x_n)$ becomes the random function used to describe the random variable. An actual realization of the random process is known as a regionalized variable (Webster and Oliver 2007). The regionalized variable is made up of three parts: (1) a structural component (with a constant mean or a trend), and a random component made up of (2) spatially correlated variation, and (3) uncorrelated noise. The random model can be written as

$$Z(x) = \mu + \varepsilon'(x) + \varepsilon'', \tag{3.2}$$

where $Z(x)$ is the random variable, μ is the mean, $\varepsilon'(x)$ is a spatially autocorrelated error component, and ε'' is a random component with a mean of zero (Burrough et al. 2015). Here, $\varepsilon'(x)$ has a covariance $C(h) = E[\varepsilon'(x)\,\varepsilon'(x+h)])$ that depends only on h, the spatial separation distance between sample points (Webster and Oliver 2007). Note that the covariance exists and depends only on h, an assumption known as second-order stationarity. A random function, however, may not meet this assumption, in which case the mean and covariance are undefined (Myers 1989). An alternative and less restrictive form of stationarity can then be used, known as the intrinsic hypothesis,

$$E[Z(x) - Z(x+h)] = 0, \tag{3.3}$$

where the expected first difference between $Z(x)$ and itself at separation distance h is zero. The variance of the difference is used instead of the covariance:

$$var[Z(x) - Z(x+h)] = 2\gamma(h), \tag{3.4}$$

where γ is the variance (also called the semivariance), and $2\gamma(h)$ is the variogram (Cressie 1993).

If the expectation of $Z(x)$ does not only depend on separation distance h, but also on position x, the random variable is not spatially stationary. In this case, the deterministic structural component must be separated from the random component (the spatially autocorrelated variation and white noise). This is accomplished through specification of a mean function in the random model:

$$Z(x) = \mu(x) + \varepsilon'(x) + \varepsilon'', \tag{3.5}$$

where $\mu(x)$ is a deterministic mean function. The typical approach for specifying a mean function is a simple linear regression of variable Z and the spatial coordinate(s). The variogram is then calculated from the residuals:

$$2\gamma(h) = E[\{\varepsilon'(x) - \varepsilon'(x+h)\}^2]. \tag{3.6}$$

The variogram, in addition to describing the spatial continuity of a random variable, is also used during interpolation to assign spatial weights in order to achieve the best linear unbiased predictor (BLUP) for a random variable Z at an unsampled point x_0. Computing the variogram allows for the weighting of sampled observations based on their distance from the unsampled point. The variogram exploits the spatial autocorrelation inherent to the data; points nearer the origin are weighted greater than more distant points. Since temperature differences are theorized to obey a power law relation to their separation distance, weighted interpolation provides a means of assessing the portions of the profile that most likely obey the theorized scaling relationship.

Finding the value of Z at x_0 (i.e., interpolation) is accomplished through a procedure known as universal kriging. BLUP is achieved through a weighted linear sum,

$$\hat{Z}x_{(0)} = \sum_{i=1}^{N} \lambda_i f_k(x_i)\,, \tag{3.7}$$

where λ_i are spatial weights, and f_k are functions of the spatial coordinates. For a one-dimensional dataset, such as the vertical profiles in this study, there are $k = 2$ covariates where $f_1 = 1$ and $f_2 = x_1$. As a condition of the unbiasedness, the weights sum to 1, $\sum_{i=1}^{N} \lambda_1 = 1$. Weights are solved, in matrix notation, as

$$A\lambda = \mathrm{b}, \tag{3.8}$$

where A is a symmetrical $(N + k) \times (N + k)$ matrix of the γ values of the residuals between all sampled points and the spatial coordinate covariates, b is a vector of γ values of the residuals between all sampled points and the unsampled point and the corresponding spatial covariates, and λ is a vector of weights and Lagrange multipliers used for optimization, which expands to

$$\begin{bmatrix} \gamma_{11} & \cdots & \gamma_{1n} & f_{11} & \cdots & f_{1k} \\ \vdots & \ddots & \vdots & \vdots & \ddots & \vdots \\ \gamma_{n1} & \cdots & \gamma_{nn} & f_{n1} & \cdots & f_{nk} \\ f_{11} & \cdots & f_{1n} & 0 & \cdots & 0 \\ \vdots & \ddots & \vdots & \vdots & \ddots & 0 \\ f_{k1} & \cdots & f_{kn} & 0 & \cdots & 0 \end{bmatrix} \times \begin{bmatrix} \lambda_1 \\ \vdots \\ \lambda_n \\ \psi_1 \\ \vdots \\ \psi_k \end{bmatrix} = \begin{bmatrix} \gamma_{10} \\ \vdots \\ \gamma_{n0} \\ f_{10} \\ \vdots \\ f_{k0} \end{bmatrix}, \tag{3.9}$$

where the Lagrange multipliers are denoted by ψ (Webster and Oliver 2007). The BLUP is found through minimization of the kriging variance

$$\sigma_k^2 = 2\sum_{i=1}^{N} \lambda_i \gamma(x_0 - x_i) - \sum_{i=1}^{N}\sum_{j=1}^{N} \lambda_i \lambda_j \gamma(x_i - x_j). \tag{3.10}$$

Materials and Methods

Study Area

The data for this study were collected on 18 July 2018 in the San Luis Valley of Colorado during the Lower Atmospheric Process Studies at Elevation - a Remotely-piloted Aircraft Team Experiment (LAPSE-RATE) field campaign as part of the International Society of Atmospheric Research using Remotely-piloted Aircraft (ISARRA) annual meeting. LAPSE-RATE was a coordinated effort that included more than 100 participants from 13 institutions and

organizations. During the six-day campaign, more than 35 unmanned aircraft were deployed and completed 1,287 flights, accumulating more than 260 flight hours to capture data for a variety of scientific objectives, including observations of the morning boundary-layer transition, the diurnal cycle of valley flows, convective initiation, and aerosol properties, among others (Barbieri et al. 2019).

Geographically, the San Luis Valley is a high-desert valley located in south-central Colorado, with an average elevation of approximately 2,300 m above mean sea level (MSL). The valley is flanked by mountain peaks exceeding 4,300 m MSL and frequently experiences convective storms during late afternoons in the summer. While flight activities for the comprehensive LAPSE-RATE campaign spanned six days and occurred at multiple locations across the valley, the data used in this study were captured at one location, Moffat, a rural area 30 km north-east of Alamosa, Colorado, at an elevation of 2,310 m MSL. While flights occurred on the grounds of a school, the vegetation immediately adjacent was dominated by deciduous shrubs.

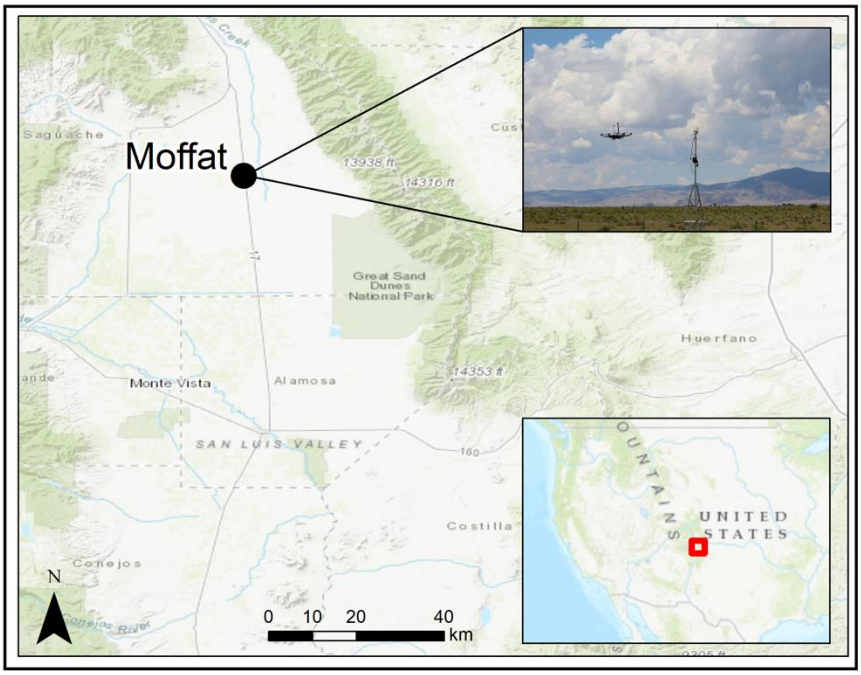

Figure 3.1. Map of the Moffat flight location in the San Luis Valley (Base map: Esri)

Flights consisted of six vertical profiles captured during the early morning and continuing through the mid-day boundary-layer transition (Table 3.1). All flights were conducted under a Certificate of Authorization (COA) issued by the Federal Aviation Administration (FAA), which allowed maximum altitude to exceed the federally mandated maximum of 123 m (400 ft.). Maximum altitudes on 18 July ranged from 490.0 – 499.7 m above ground level (AGL). Ascent speeds averaged 3.3 m s^{-1}.

Flight #	Start Time	End Time	Max Alt AGL [m]
1	07:08:02	07:10:48	490.9
2	07:59:41	08:02:42	499.2
3	08:59:43	09:02:45	499.2
4	10:59:56	11:01:48	499.7
5	11:46:50	11:49:47	498.2
6	12:29:02	13:01:02	499.1

Table 3.1. Flight times and maximum altitudes for the 12 profiles. All times are local (UTC – 6 h).

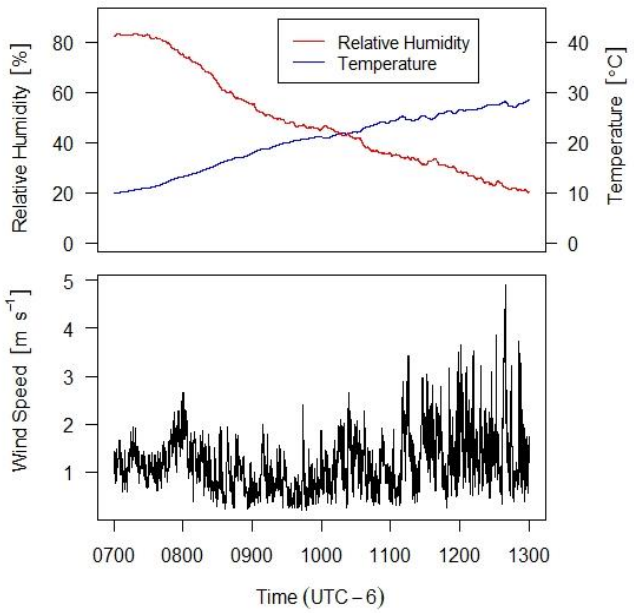

Figure 3.2. Surface weather conditions at the Moffatt flight location, measured approximately 3 m AGL

Surface Weather Conditions at the Study Location

Surface weather conditions at the Moffat site were recorded by a meteorological tower approximately 3 m in height (Figure 3.2). Temperature, relative humidity, pressure, and wind speed and direction (not shown) were recorded throughout the duration of flight activities. The temperature at the surface ranged from approximately 10° C at 0700 local time (LT, UTC -6 h) to nearly 30° C by 1300 LT. Relative humidity decreased from 80% at 0700 LT to roughly 10% by 1300 LT. Winds were calm in the morning at roughly 1 m s^{-1}, increasing to speeds of up to 5 m s^{-1} by the early afternoon.

Radiosonde Measurements

In addition to the surface weather observations, radiosondes were deployed several times throughout the day. Profiles of potential temperature and wind speed captured at three different times throughout the flight activities show a slight inversion during the 0830 LT radiosonde above approximately 200 m AGL. The 1001 LT radiosonde profile shows a slight inversion at around 500 m, and the 1131 LT profile indicates a mixed boundary layer.

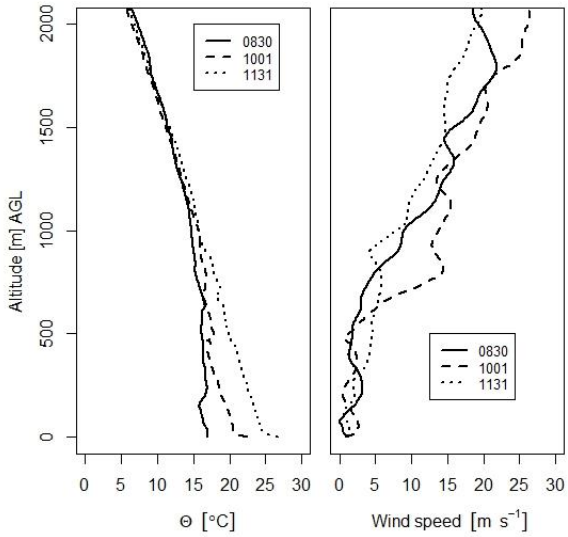

Figure 3.3. Radiosonde potential temperature [Θ] and wind speed profiles

Aircraft and Instrumentation

The aircraft platform was a DJI Matrice 600 (DJI Shenzhen, Guangdong, China). The Matrice 600 is a hexacopter measuring 1.13 m in diameter and weighing 9.1 kg. The platform has a 7 kg payload capacity and is therefore capable of accommodating larger meteorological instruments. The Matrice 600 was outfitted with a Young Model 81000 (R. M. Young Company, Traverse City, MI) ultrasonic anemometer weighing 1.2 kg, which was affixed to the aircraft using custom designed mounts (Figure 3.4). Vehicle telemetry and atmospheric observations were synchronized and logged at 32 Hz onto a Stabilis flight control module developed at Oklahoma State University (Donnell et al. 2018). The resulting aggregate is referred to as a WxUAS.

Figure 3.4. DJI Matrice 600 hexacopter outfitted with a Young Model 81000 ultrasonic anemometer on top (Photo: Jamey Jacob).

The placement of the anemometer centrally on the aircraft and above the propellers (Figure 3.4) minimizes effects of rotor downwash, although contamination may occur during high descent rates due to rotor downwash and separation over the WxUAS fuselage (Avery et al. 2019), which limits data collection to during hover and ascent flight modes. Consequently, only data collected during the ascent were analysed in an effort to ensure temporal stationarity and limit interference from the aircraft. The anemometer was validated, while flying on the platform,

against the Mobile UAS Research Collaboratory (MURC), which is a ground-based system operated by the University of Colorado-Boulder's Integrated Remote and In-Situ Sensing (IRISS) program that provides instrumentation for reference comparisons. The MURC has a 15 m extendable mast hosting a suite of meteorological sensors. The Young 81000 mounted on the WxUAS compared well against the MURC measurements while flying at 15 m for a sustained period of 8 minutes (Barbieri et al. 2019).

Calculation of Sonic Temperature

This study utilized sonic temperature measurements captured with the Young Model 81000 ultrasonic anemometer. Sonic temperature can be determined through the calculation of the speed of sound, which is done through the transit time method (Brock and Richardson 2001). An acoustic pulse is emitted in opposing directions between two transducers, and the speed of sound can be determined through the equation

$$c = \frac{d}{2}\left(\frac{1}{t_1} - \frac{1}{t_2}\right), \tag{3.11}$$

where c is the speed of sound, t_1 and t_2 are the transit times of the acoustic pulse between opposing transducers, respectively, and d is the distance between the transducers. Sonic temperature can then be computed directly using the speed of sound

$$T = c^2 kR, \tag{3.12}$$

where T is sonic temperature, k is the ratio of specific heat of air, and R is the specific gas constant. When water vapor pressure is low compared to the atmospheric pressure, sonic temperature becomes a good approximation to the actual air temperature. In typical conditions, error can be less than 1% (Harrison 2015).

On a three-axis sonic anemometer, such as the Young 81000, sonic temperature is computed using the vertical, w, velocity component. The speed of sound calculation is independent of wind speed in the direction parallel to the acoustic pulse. Consequently, the

vertical motion of the aircraft should have negligible effects on the calculation of the speed of sound and, thus, sonic temperature.

In previous studies, good agreement has been obtained between temperature measurements from sonic anemometers and fast-response hot-wires, demonstrating the applicability of this technique (Schotanus et al. 1983). In addition, observed values of C_2 from an sUAS compared well with other measurements (in this case, sodar), but differed from numerical predictions, potentially due to site-specific characteristics such as topography (Wainwright et al. 2015). In previous studies (van den Kroonenberg et al. 2012; Braam et al. 2016) the horizontal profiles of temperature obtained from the sUAS were treated as a time series and converted to the spatial domain through the application of Taylor's hypothesis and the mean ground speed or the true air speed. Profiles in the present study were treated as a true spatial series.

Estimates of C_2 are sensitive to the time constant of the temperature sensor, that is, the time it takes the sensor to respond to a new temperature value. A sensor time constant smooths the data and can result in lowering C_2 estimates by as much as 5% (Platis et al. 2016). Wainwright et al. (2015) applied a correction to account for the sensor time constant. In contrast, sonic temperature used in this study has no appreciable time delay in adjusting to the speed of sound and thus sonic temperature. The time constant is effectively the sampling rate, which was 32 Hz.

Estimating Sample Variograms

Sample variograms $2\hat{\gamma}(h)$ were estimated from the temperature profiles using the method-of-moments estimator:

$$2\hat{\gamma}(h) = \frac{1}{N(h)} \sum_{i=1}^{N(h)} \{Z(\boldsymbol{x_i}) - Z(\boldsymbol{x_i} + h)\}^2 , \tag{3.13}$$

where $Z(\boldsymbol{x_i})$is the observed value at location x_i and $Z(x_i + h)$ is the observed value at location x_i separated by distance h. N is the number of sample pairs at each separation distance (Cressie

1993). The variogram estimator (Equation 3.13) was applied to the residuals of the mean function as specified in Section 2. Residuals were discretized into bins based on their spatial separation distance from one another. A bin width of 1 m was selected as a compromise between variogram clarity and the ability to capture the variable structure. Bins were set every 1 m up to 100 m separation distances.

Fitting Model Variograms

Sample variogram data are typically modelled to mitigate the influence of noise and scatter (Webster and Oliver 2007). The power model variogram is defined as

$$2\gamma(h) = C_0 + C_2 h^{\alpha}, \tag{3.14}$$

where α is a scaling exponent, and C_0 is an error component known as the nugget effect. In many cases, the variogram may intersect the *y* axis at a point greater than zero. This is attributed to micro-structure of the data smaller than that of the sampling distance, measurement error, or spatial positioning errors (Chiles and Delfiner 2012). The power model variogram is only valid when $0 > \alpha > 2$ (Webster and Oliver 2007). A value of $\alpha = 1$ would result in a linear variogram. Power model variograms were fit to the sample variograms using weighted non-linear least squares with α fixed to 2/3 following the theory of Kolmogorov (1941a). The weights are given by $N(h)/2\gamma(h)^2$, where N is the number of point-pairs in the sample variogram estimate, which allows greater weight to be given to sample variogram point-pairs nearer the origin.

Universal Kriging and Quantitative Assessment of Model Fit

While comparisons between the sample and modelled variograms can indicate the separation distances at which the inertial range can be resolved using the theorized scaling relationship, they do not allow for a localized determination of how the modelled variogram fits the data. To quantitatively assess model fit, universal kriging was used to estimate values across the profile and then cross-validated those estimates against the modelled values. Due to the very high density of the data points (32 Hz), a stratified random sample of observations was selected

such that there was at least one observation selected per meter in altitude across the entirety of the profiles. Universal kriging was then performed using the fitted 2/3 power law model variogram for weight assignment as described in Section 3.2.

Model fit was assessed through the cross-validation of the universal kriging estimates. A leave-one-out, cross-validation procedure was implemented such that each observation was iteratively excluded from the sample, and its temperature value was predicted using the remaining observations. This process was repeated until temperature estimates for all observations were obtained. The statistic used to measure the goodness of the model variograms was the mean square deviation ratio

$$MSDR = \frac{1}{N}\sum_{i=1}^{N}\frac{\{Z(\boldsymbol{x}_i) - \hat{Z}(\boldsymbol{x}_0)\}^2}{\sigma^2(\boldsymbol{x}_i)}, \tag{3.15}$$

where $Z(\boldsymbol{x}_i)$ is the measured temperature value, $\hat{\boldsymbol{Z}}\boldsymbol{x}_{(0)}$ is the temperature estimate, and $\hat{\sigma}^2(\boldsymbol{x}_i)$ is the estimated kriging variance. If the model variogram fits the data well, the kriging variance and the squared residual of the estimate will be close in value, resulting in an MSDR near 1 (Webster and Oliver 2007). A profile of the SDR value at every prediction location provides a localized assessment of model fit. Analysis was completed using the gstat package (Pebesma 2004) in the R statistical computing language.

Results

Profiles

Temperature profiles (Figure 3.5) show the progression of the ABL throughout the morning transition. The first two profiles exhibit an increase in temperature with altitude suggesting the remnants of a stable nocturnal boundary layer. The four subsequent profiles, occurring from 0859–1259 LT, are indicative of the boundary-layer transition to a mixed state as the morning progressed into the early afternoon. The two middle WxUAS profiles, 0859 LT and 1059 LT, display very little variability about their mean compared to the others. The penultimate

WxUAS profile displays a slight increase in temperature between 10 and 40 m AGL as well as a relative increase in temperature between 100 m and 200 m AGL. This increase in temperature begins sharply and may be an artefact of the sensor. Similarly, the final WxUAS profile depicts a similar segment with an increase in temperature between approximately 30 and 80 m AGL.

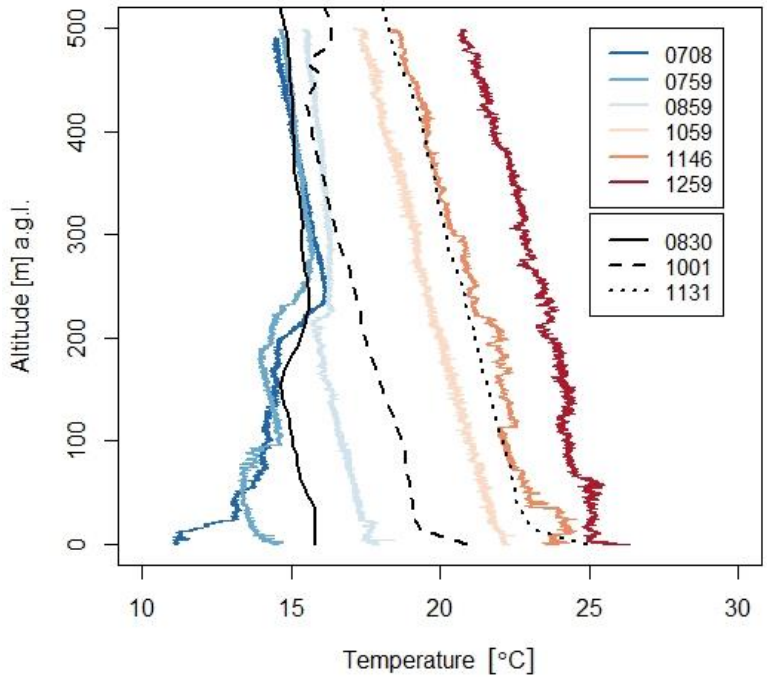

Figure 3.5. Temperature profiles captured by sUAS (colored lines) and radiosondes (black lines). Radiosonde profiles are not displayed as Θ, but in temperature for comparison to the sonic temperature profiles captured by the WxUAS. All times are local (UTC -6 h).

The radiosonde profiles of temperature (Figure 3.5, black lines) display relative agreement with the sonic temperature profiles captured with the WxUAS. The profile of the 0830 LT radiosonde depicts the same increase in temperature with altitude at roughly 200 m AGL as the 0708 LT and 0759 LT WxUAS profiles. The 1001 LT radiosonde profile shows a smooth decrease in temperature with altitude, similar to the 0859 LT and 1059 LT WxUAS profiles. The 1131 LT profile also shows a smooth decrease in temperature with altitude, unlike the nearly

contemporaneous 1146 LT WxUAS profile, which shows greater variability about the mean. This difference is likely a result of the low resolution of the radiosonde data having a smoothing effect.

Variograms

Variograms estimated from data from the six WxUAS profiles (Figure 3.6) reveal a variety of structural characteristics. Recall that in the inertial range, the sample variogram should closely follow the 2/3 power law model variogram (Equation 3.14). The model variogram, which has been forced to follow 2/3 power, is represented with the solid red line; sample variograms are represented by the black circles (Figure 3.6).

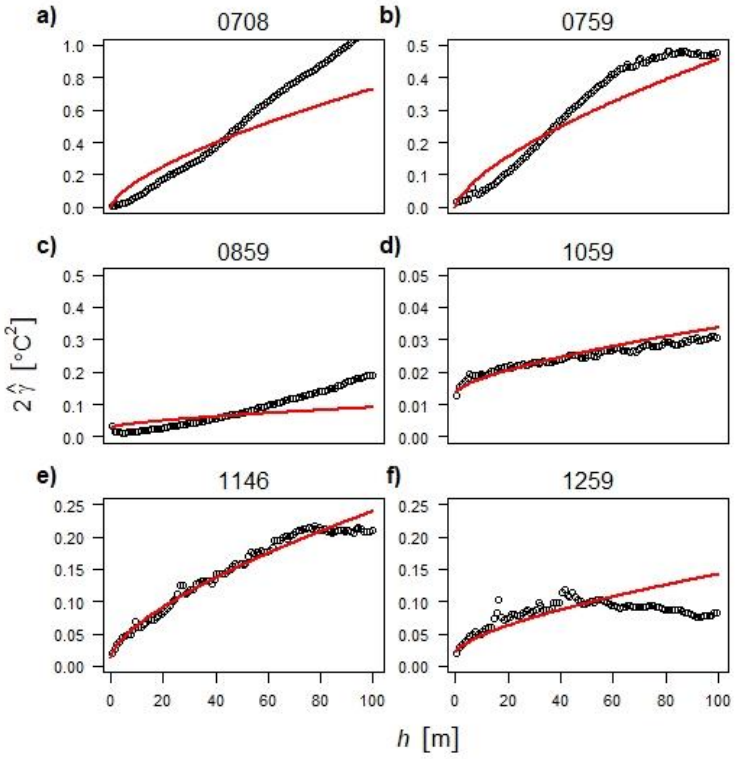

Figure 3.6. Sample variograms (circles) and fitted 2/3 power law model variograms (red lines) for all full profiles (h is vertical separation distance between sample pairs, and $2\hat{\gamma}$ is the variogram)

To identify the sample separation distances that are inherent to the inertial subrange of turbulence and assess the degree of deviation from the theoretical 2/3 power law scaling relationship, sample variogram fits were assessed visually and also quantitatively measured fit via the MSDR between the sample and modelled variograms. The 2/3 power law model variograms

do not fit the first three profiles well (Figs. 6a–c). The sample variograms increase as a function of distance at a greater rate than that of the model variogram for Flights 1–3. C_2 and C_0 estimates are reported in Table 3.2 but are not meaningful considering the data do not fit the model. The MSDR is therefore not reported for these three flights. The 2/3 power law model variograms fit profiles from Flights 4–5 well, as the sample variogram follows the model variogram closely throughout the 100 m range of separation distances (Figure 3.6d, e). A nugget effect, C_0, was estimated on these two models, with values of 0.014 °C^2 for both. C_2 estimates for Flights 4–5 were 0.001 °C^2 m $^{-2/3}$ and 0.010 °C^2 m $^{-2/3}$, respectively. Flight 4 had an MSDR of 0.993, meaning the 2/3 power law model fit the data quite well, whereas Flight 5 had an MSDR of 0.53, indicating a moderate fit. The model variogram fit the final profile, Flight 6, well up to roughly the 50 m separation distance, but then the sample variogram began to decrease with distance until the maximum separation distance of 100 m was reached (Figure 3.6f). The C_2 estimate for Flight 6 decreased from the previous flight to 0.006 °C^2 m $^{-2/3}$. A C_0 value of 0.022 °C^2 was estimated for Flight 6, and the MSDR was 0.677 (Table 4.2).

Flight #	C_2	C_0	α	MSDR
1	0.034	0.000	2/3	-
2	0.021	0.000	2/3	-
3	0.003	0.027	2/3	-
4	0.001	0.014	2/3	0.993
5	0.010	0.014	2/3	0.539
6	0.006	0.022	2/3	0.677

Table 3.2. Variogram parameter estimates and fit diagnostic for Flights 1–6.

Computing the structure function across the full extent of Flights 1–3 is likely not appropriate given the slight inversion in the profiles at roughly 250 m AGL. To account for this inversion, the variogram and its parameters were estimated for Flights 1–3 from the data below 250 m AGL and above 250 m AGL separately, and the results are presented in Figure 3.7 and Table 3.3.

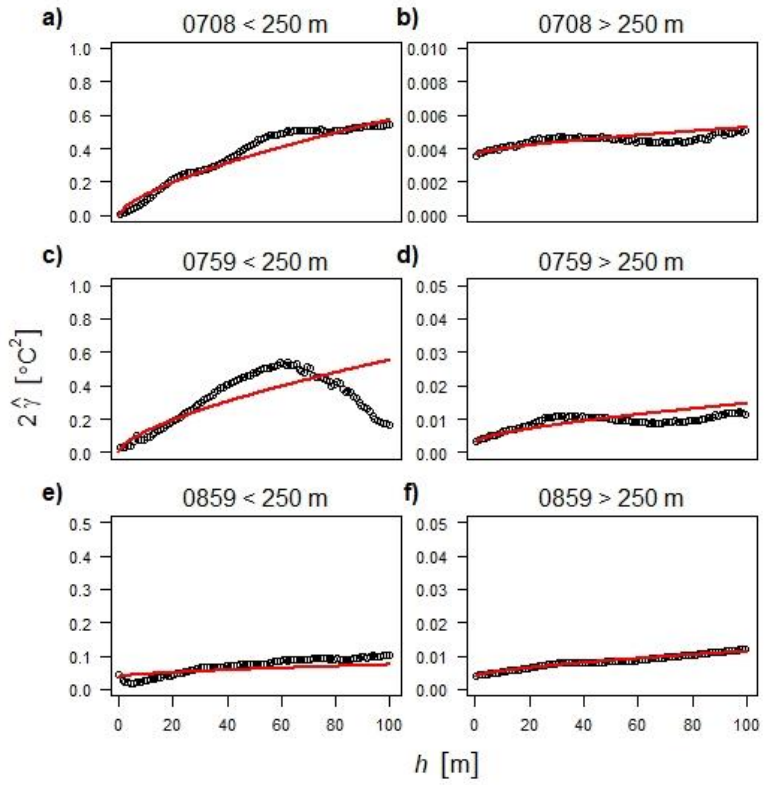

Figure 3.7. Sample variograms (points) and fitted 2/3 power law model variograms (lines) for 0708, 0759, and 0859 profiles for altitudes above and below 250 m AGL. (h is vertical separation distance between sample pairs, and $2\hat{\gamma}$ is the variogram)

Variograms estimated from the lowest 250 m AGL from the first three profiles display very different structural behavior than the variograms estimated from 250 m AGL and above. The variogram estimated from Flight 1a roughly follows the 2/3 power law model variogram with a slight deviation between 40 and 80 m separation distances (Fig 7a). C_2 was estimated to be 0.027 $°C^2\ m^{-2/3}$, and a C_0 value was not fit. The MSDR was estimated to be 0.309. The variogram for Flight 2a increases at a rate greater than the 2/3 power law model variogram (Figure 3.7c). The variogram peaked at a separation distance of about 60 m, and then the variogram began to decrease. The variogram of Flight 3a roughly follows the 2/3 power law model (Figure 3.7e), but the C_2 value was estimated to be 0.002 $°C^2\ m^{-2/3}$, nearly one-tenth the value of C_2 estimated from Flights 1a and 2a. A C_0 was estimated to be 0.038 $°C^2$, and the MSDR was estimated to be 0.286, suggesting the model was poorly fit. The variograms for Flights 1b, 2b, and 3b all appear

similarly flat (Figures 3.7b, 3.7d, 3.7f) and had similar estimates of C_0. Flight 1b had a C_2 estimate near zero, while flights 2b and 3b had C_2 estimates of 0.001 °C^2 m$^{-2/3}$and 0.002 °C^2 m$^{-2/3}$, respectively.

Flight #	C_2	C_0	α	MSDR
1a	0.027	0.000	2/3	0.309
1b	0.000	0.004	2/3	1.067
2a	0.025	0.007	2/3	1.086
2b	0.001	0.003	2/3	1.086
3a	0.002	0.038	2/3	0.286
3b	0.000	0.004	2/3	0.858

Table 3.3. Variogram parameter estimates and fit diagnostic for Flights 1–3 (a) below 250 m AGL and (b) above 250 m AGL.

Cross-Validation of Kriging Estimates

To distinguish specific altitudes for which the scaling relationship is valid, universal kriging estimates of the temperature profiles using weights assigned by the 2/3 power model variogram were assessed. As a localized measure of how well the 2/3 power law variogram fit the data, the SDR was estimated at every meter along the profiles using the method described in Section 3.8. As with the MSDR statistic, local SDR estimates near 1 indicate the model variogram fit the data well, meaning that the inertial range at that location was well resolved through theorized scaling. Flights 1–3 were analyzed in the sections above and below 250 m AGL separately, using the variogram parameters listed in Table 3.3. SDR estimates from Flights 1a, 2a, and 3a are less than 1 throughout the extent of the 250 m subset of the profile (Figure 3.8). SDR estimated from Flight 1b oscillates, crossing 1 several times along the extent of the profile subset. Flight 2b SDR estimates hover near 1 between 300 and 400 m AGL and then remain below 1 throughout the extent of the profile. Flight 3b SDR estimates display a similar pattern to those of 2b, having values near 1 in the portion of the profile near 300 m AGL and dropping below 1 as the profile approaches its maximum extent near 500 m AGL.

Recall that Flight 4 had the best MSDR value of 0.993. This fit is similarly reflected in the local SDR estimates along the profile. The smoothing spline closely follows a value of 1, with slight deviations near 150 m and 350 m AGL Flight 5, with an MSDR of 0.539, displays local SDR estimates of less than 1 throughout the extent of the profile, with the exception of the lowest 50 m AGL Flight 6, with an MSDR of 0.677, is slightly more representative of the 2/3 power law model variogram than Flight 5. Local SDR estimates roughly follow a value of 1 until 300 m AGL, where they dip below 1 for the remainder of the profile.

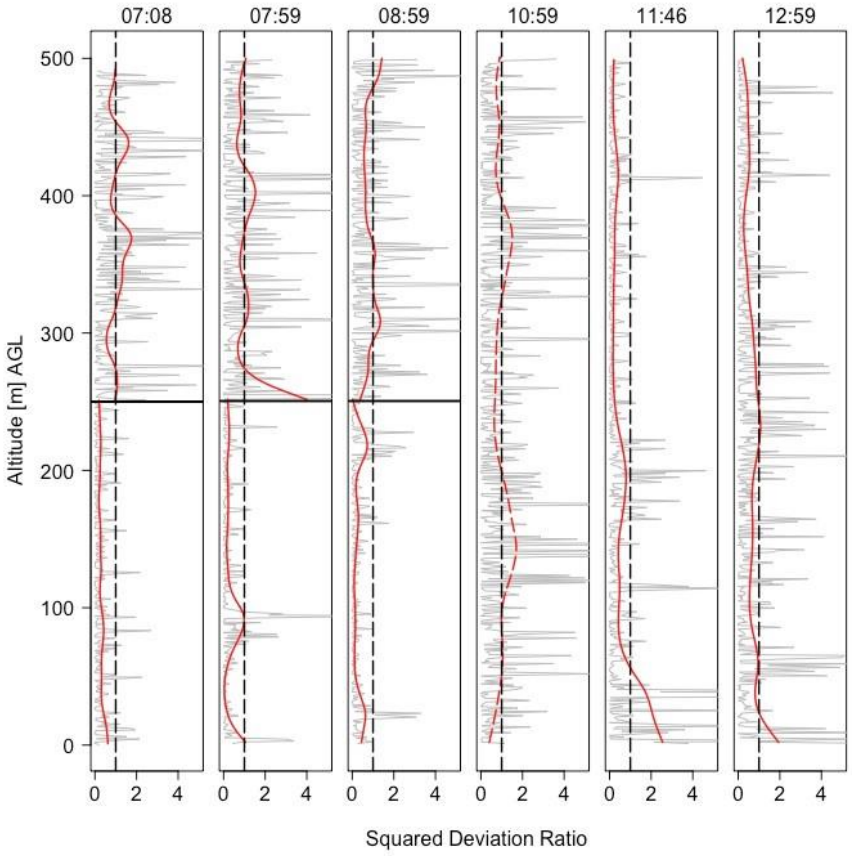

Figure 3.8. SDR profiles of kriging estimates (gray lines) and smoothing splines (red lines). Dashed lines are the ideal ratio of 1.

In summary, the 2/3 power model variogram fit Flights 4–5 well across the entire range of separation distances. The model fit Flight 6 well for a large portion of the separation distances, up to 50 m (Figure 3.6). For Flights 1–3, the presence of an inversion forced the need to separate

the measurements into two groups: below 250 m AGL and above 250 m AGL After this was done, the 2/3 power law model variogram visually appeared to fit the sample variogram well in Flight 1a and 3a (Figs. 7a, e), but when fit was measured quantitatively through SDR, the result indicated these flights were poorly fit, resulting in poor estimates. The variogram of Flight 2a appeared to have a wave-like nature (Fig 7c), indicative of periodicity in the data. Results from this portion of the analysis suggest that the 2/3 model variogram fit to the residual process of a temperature profile can be used to identify sample separation distances inherent to the inertial subrange in well-mixed conditions. However, the model was less successful in resolving the inertial subrange in the early morning flights, particularly below the slight temperature inversion.

The degree of deviation from the theorized second-order scaling relationship inherent to the inertial subrange of turbulence was assessed through cross-validation of universal kriging. It was determined that during stable, early morning ABL conditions (with altitudes < 250 m AGL), the process is less variable (i.e., less random) than the 2/3 power law model, which led to the SDR values to be less than 1 along the extent of these profiles. The subsequent three flights occurring later in the morning exhibited temperature scaling that was more consistent with the theorized 2/3 power law model. The theorized scaling was present along most of the profile from Flight 4 and on Fights 5–6 at altitudes from roughly 50–200 m AGL.

Discussion

While turbulence in the inertial subrange is considered to be isotropic and spatially stationary (i.e., homogenous), the vertical profiles of temperature from which turbulent fluctuations can be inferred are not spatially stationary. Thus, they require a modified form of the structure function to account for the non-constant mean across the spatial domain. Geostatistical approaches are well-suited for modeling random variables experiencing nonstationarity. In this study, the aim was to characterize the vertical structure of temperature profiles captured via WxUAS using geostatistical tools and more specifically: (1) use the variogram to identify sample separation distances that are inherent to the inertial subrange of turbulence, (2) assess the degree

of deviation from the theoretical 2/3 power law scaling relationship, and (3) distinguish specific altitudes for which the scaling relationship can be resolved through universal kriging estimates of the temperature profiles using weights assigned by the 2/3 power model variogram.

Resolution of Theorized Scaling and Model Fit

In pursuit of these objectives, it was found that after detrending the data to account for the nonstationary mean, the fitted 2/3 power law model variograms were generally successful in modeling the spatially autocorrelated error components of the random variable (temperature), particularly in well-mixed conditions, thereby allowing us to identify sample separation distances that were inherent to the inertial subrange of turbulence. An analysis of the behavior of the spatial autocorrelation can lead to a better understanding of the relationship between the power law scaling parameter and the process being modelled.

Power law model variograms (Equation 3.14) are valid when the scaling exponent is $0 < \alpha < 2$. When $\alpha = 1$, the variogram is linear, and successive increments are stationary and independent. The limits of α, 0 and 2, represent a constant variance for all *h* and differentiable, non-random variation, respectively. As α approaches 2, the variogram becomes increasingly parabolic, whereas an α near zero is indicative of a white-noise process (Webster and Oliver 2007). A more thorough understanding of the autocorrelation may be achieved through what Mandelbrot and Van Ness (1968) describe as fractional Brownian motions (fBm). In an fBm, successive increments are autocorrelated. When $\alpha > 1$, the increments are positively correlated, meaning they tend to move in the same direction. Conversely, when $\alpha < 1$, the error increments are negatively correlated, meaning they tend to move in opposite directions (Webster and Oliver 2007). Few processes in nature are represented by a power law with $\alpha < 1$, but turbulence is a notable exception. The negative spatial autocorrelation inherent to inertial range turbulence makes its spatial prediction challenging.

Flight 1a, below 250 m AGL, displays temperature scaling that follows the 2/3 power law model. The variogram of the subsequent Flight 2a estimated from data below 250 m AGL is more parabolic in nature, and beyond 60 m separation distances, measured temperature values become increasingly similar. Such behavior in measured autocorrelation is indicative of a periodic or oscillatory process. Indeed, parabolic behavior of the variogram is often seen in physical processes influenced by gravity (Chiles and Delfiner 2012). Gravity waves are often present in a weakly turbulent stable boundary layer (Stull 1988), and high wind shear is known to induce Kelvin–Helmholtz waves. This phenomenon was observed by Higgins et al. (2018) using distributed temperature sensing to profile the stable boundary layer using an sUAS. The precise cause of the periodic behavior in the vertical variogram cannot be fully characterized in this study and is thus an opportunity for further research.

Periodicity was not observed in the subsequent variogram of Flight 3 at 0859 LT, and C_2 was estimated to be roughly an order of magnitude less than the previous flight. C_2 estimated from Flight 4 was similarly low. The 1001 LT radiosonde wind speed profile captured in the time between Flights 3–4 suggests the presence of geostrophic winds with speeds in excess of 15 m s^{-1} at approximately 900 m AGL (Figure 3.3). Van den Kroonenberg et al. (2012) attributed higher C_2 estimates aloft to the presence of a low-level jet (LLJ). In contrast, lower C_2 estimates from the two WxUAS profiles bounding the LLJ were observed.

The 2/3 power law model fit the variograms estimated from the data of Flights 4–6, indicating fully developed isotropic turbulence in the ABL. The C_2 estimate increased by roughly an order of magnitude between Flights 4–5, then decreased slightly by Flight 6 at 1259 LT. Typically C_2 increases until approximately midday and then begins to decrease (van den Kroonenberg et al. 2012). C_2 estimates from the final three flights behaved in accordance with this assumption. A nugget variance, C_0, was fit to the final three flights as well. The more turbulent nature of the profile, as indicted by the variogram closely following the α value of 2/3, likely leads to greater discontinuity at the variogram's origin. Recall that α values less than 1 are

representative of a process whose successive increments are negatively autocorrelated (i.e., more dissimilar). This roughness of the data likely contributed to the presence of the nugget variance.

Profile Estimation Using Universal Kriging

An SDR estimate of less than 1 indicates that the squared residual is less than the estimated kriging variance. This is an indication that the process being modelled is less variable than predicted. Kriging has the effect of smoothing the data, thus SDR estimates (and MSDR estimates) are expected to be below 1 even if the model is well fit to the data. Nevertheless, the SDR estimates are below 1 for nearly the full extent of profiles from Flights 1a, 2a, and 3a, meaning that the process is less variable (i.e., less random) than the 2/3 power law model. SDR estimates from Flights 1b, 2b, and 3b are more variable than the model (values greater than 1). This suggests that estimation of the variogram from vertical profiles is sensitive to both the maximum separation distances for which it is estimated, as well as the vertical domain. The upper limit of the boundary layer is not well defined under stable conditions (Stull 1988), and entrainment processes have influence on the spatial autocorrelation of the temperature measurements therein. SDR estimates from the final three flights were more successful in identifying portions of the profile when theorized temperature scaling was valid due to the turbulence being more well developed.

Conclusions

Variograms were estimated from vertical profiles of temperature collected throughout the morning boundary-layer transition across two days in the San Luis Valley, CO. To account for the variation in temperature with altitude, a mean function was specified and the variogram was estimated from the residuals. Power law model variograms with a 2/3 scaling exponent were fit to the sample variograms to assess the separation distances commensurate with the inertial range of turbulence and correspondingly, estimate the temperature structure parameter, C_2. Geostatistical methods for spatially nonstationary random variables were well suited to describe the vertical structure of temperature in the ABL. The variogram estimated from the residuals allowed for the

resolution of the inertial subrange of turbulence. Local variance estimates obtained through cross-validation of universal kriging estimates allowed for identification of portions of the temperature profiles that conform to the theorized inertial subrange temperature scaling relationship. It was found that this relationship was not well resolved under stable conditions. Results are likely sensitive to maximum separation distances and the extent for which the variogram is estimated.

References

Antonia, R.A., Hopfinger, E.J., Gagne, Y., & Anselmet, F. (1984). Temperature structure functions in turbulent shear flows. *Physical Review A*, *30*(5), 2704.

Avery, A.S., Whyte, S., Brenner, J., Natalie, V.A., & Jacob, J.D. (2019) Experimental Measurement of Flow Field Around a Rotary Wing Unmanned Aircraft for Evaluation of Onboard Anemometer Placement, 72nd Annual Meeting of the APS Division of Fluid Dynamics.

Barbieri, L., Kral, S.T., Bailey, S.C., Frazier, A.E., Jacob, J.D., Reuder, J., ... & Doddi, A. (2019). Intercomparison of small unmanned aircraft system (sUAS) measurements for atmospheric science during the LAPSE-RATE campaign. *Sensors*, *19*(9), 2179.

Bonin, T.A., Goines, D.C., Scott, A.K., Wainwright, C.E., Gibbs, J.A., & Chilson, P.B. (2015). Measurements of the temperature structure-function parameters with a small unmanned aerial system compared with a sodar. *Boundary-Layer Meteorology*, *155*(3), 417–434.

Braam, M., Beyrich, F., Bange, J., Platis, A., Martin, S., Maronga, B., & Moene, A.F. (2016). On the discrepancy in simultaneous observations of the structure parameter of temperature using scintillometers and unmanned aircraft. *Boundary-Layer Meteorology*, *158*(2), 257–283.

Brock, F. & Richardson, S. (2001). *Meteorological measurement systems*. New York: Oxford.

Burrough, P.A., McDonnell, R., McDonnell, R.A., Lloyd, C.D. (2015). *Principles of Geographical Information Systems*, 3rd ed; Oxford University Press: New York.

Calmer, R., Roberts, G., Preissler, J., Derrien, S., & O'Dowd, C. (2018). Vertical wind velocity measurements using a five-hole probe with remotely piloted aircraft to study aerosol–cloud interactions. *Atmospheric Measurement Techniques*.

Chiles, J-P, & Delfiner, P. (2012) Geostatistics: modeling spatial uncertainty. New York: Wiley.

Cioni, S., Ciliberto, S., & Sommeria, J. (1995). Temperature structure functions in turbulent convection at low Prandtl number. *EPL (Europhysics Letters)*, *32*(5), 413.

Cressie, N. (1990). The origins of kriging. *Mathematical geology*, *22*(3), 239–252.

Cressie, N. (1993). *Statistics for spatial data*. Hoboken, NJ: Wiley.

Donnell, G.W., Feight, J.A., Lannan, N., & Jacob, J.D. (2018). Wind characterization using

onboard IMU of sUAS, AIAA Aviation.

Gawędzki, K., & Kupiainen, A. (1995). Anomalous scaling of the passive scalar. *Physical review letters*, *75*(21), 3834.

Grossmann, S., & Lohse, D. (1994). Scale resolved intermittency in turbulence. *Physics of fluids*, *6*(2), 611–617.

Harrison, R. G. (2015). Meteorological measurements and instrumentation. Ney York: Wiley.

Higgins, C. W., Wing, M. G., Kelley, J., Sayde, C., Burnett, J., & Holmes, H. A. (2018). A high resolution measurement of the morning ABL transition using distributed temperature sensing and an unmanned aircraft system. *Environmental Fluid Mechanics*, *18*(3), 683–693.

Jacob, J. D., Chilson, P. B., Houston, A. L., & Smith, S. W. (2018). Considerations for atmospheric measurements with small unmanned aircraft systems. *Atmosphere*, *9*(7), 252.

Koch, S. E., Fengler, M., Chilson, P. B., Elmore, K. L., Argrow, B., Andra Jr, D. L., & Lindley, T. (2018). On the use of unmanned aircraft for sampling mesoscale phenomena in the preconvective boundary layer. *Journal of Atmospheric and Oceanic Technology*, *35*(11), 2265–2288.

Kolmogorov, A.N. (1941a). The local structure of turbulence in incompressible viscous fluid for very large Reynolds numbers. *Cr Acad. Sci. URSS*, *30*, 301–305.

Kolmogorov, A.N. (1941b). Interpolation and extrapolation of stationary sequences. *Izvestiya the Academy of Sciences of the USSR, Ser Math*, *5*: 3–14.

Konrad, T., Hill, M., Rowland, R., & Meyer, J. (1970). A small, radio-controlled aircraft as platform for meteorological sensors. *Johns Hopkins APL Tech Dig* 10: 11–19.

Lee, T. R., Buban, M., Dumas, E., & Baker, C. B. (2017). A new technique to estimate sensible heat fluxes around micrometeorological towers using small unmanned aircraft systems. *Journal of Atmospheric and Oceanic Technology*, *34*(9), 2103–2112.

Matheron, G. (1963). Principles of geostatistics. *Economic geology*, *58*(8), 1246-1266.
Mandelbrot, B. B., & Van Ness, J. W. (1968). Fractional Brownian motions, fractional noises and applications. *SIAM review*, *10*(4), 422–437.

Marusic, I., & Heuer, W.D. (2007). Reynolds number invariance of the structure inclination angle in wall turbulence. *Physical review letters*, *99*(11), 114504.

Mathieu, J, & Scott, J. (2000). *An introduction to turbulent flow*. Cambridge: Cambridge University Press.

Monin, A.S. & Yaglom, A.M. (1975). *Statistical fluid mechanics*. Cambridge: MIT Press.

Myers, D.E. (1989). To be or not to be... stationary? That is the question. *Mathematical Geology*, *21*(3), 347–362.

Obukhov, A.M. (1949). Structure of the temperature field in turbulent flow. *Geogr i Goofiz* 2(1): 58-69.

Pebesma, E.J. (2004). Multivariable geostatistics in S: the gstat package. *Computers & geosciences*, *30*(7), 683–691.

Platis, A., Altstädter, B., Wehner, B., Wildmann, N., Lampert, A., Hermann, M., ... & Bange, J. (2016). An observational case study on the influence of atmospheric boundary-layer dynamics on new particle formation. *Boundary-Layer Meteorology*, *158*(1), 67–92.

Platis, A., Moene, A.F., Villagrasa, D.M., Beyrich, F., Tupman, D., & Bange, J. (2017). Observations of the Temperature and Humidity Structure Parameter Over Heterogeneous Terrain by Airborne Measurements During the LITFASS-2003 Campaign. *Boundary-Layer Meteorology*, *165*(3), 447–473.

Smith M. (2011) Warnings: The true story of how science tamed the weather. Austin: Greenleaf Press.

Schotanus, P., Nieuwstadt, F., & De Bruin, H.A.R. (1983). Temperature measurement with a sonic anemometer and its application to heat and moisture fluxes. *Boundary-Layer Meteorology*, *26*(1), 81–93.

Sreenivasan, K.R., & Antonia, R.A. (1997). The phenomenology of small-scale turbulence. *Annual review of fluid mechanics*, *29*(1), 435–472.

Stull, R.B. (1988). *An introduction to boundary layer meteorology*. Dordrecht: Kluwer Academic Publishers.

Taylor, G.I. (1938). The spectrum of turbulence. *Proc R Soc London Ser A 164*: 476–490.

van den Kroonenberg, A. C., Martin, S., Beyrich, F., & Bange, J. (2012). Spatially-averaged temperature structure parameter over a heterogeneous surface measured by an unmanned aerial vehicle. *Boundary-layer meteorology*, *142*(1), 55–77.

Vindel, J.M., Yagüe, C., & Redondo, J.M. (2008). Structure function analysis and intermittency in the atmospheric boundary layer. *Nonlinear Processes in Geophysics*, *15*(6).

Wainwright, C.E., Bonin, T.A., Chilson, P.B., Gibbs, J.A., Fedorovich, E., & Palmer, R.D. (2015). Methods for evaluating the temperature structure-function parameter using unmanned aerial systems and large-eddy simulation. *Boundary-Layer Meteorology*, *155*(2), 189–208.

Webster R. & Oliver M.A. (2007). *Geostatistics for environmental scientists*. New York: Wiley.

CHAPTER IV

ASSESSING THE UNIVERSALITY OF THE TEMPERATURE STRUCTURE PARAMETER IN THE ATMOSPHERIC BOUNDARY LAYER

Introduction

Understanding of the mechanisms by which heat and momentum are transported in the atmosphere is of critical importance for development of accurate climate models and weather forecasting. The atmospheric boundary layer (ABL) is characterized by the presence of turbulence. Responsible for the distribution of heat and moisture in the ABL, turbulence is generated through shear as the mean wind contacts the rough surface, and through buoyancy as warm air rises as a consequence of radiative surface heating during the day (Stull 1988). The seemingly random swirls, called eddies, that comprise a turbulent flow scale from a few millimeters to the approximate depth of the ABL (~ 1 km). Richardson (1992) purported that energy entered the system through the largest turbulent motions and cascaded down to the smallest eddies through inertia where it is dissipated as heat through viscosity at the smallest scales (Pope 2000).

The random nature of turbulence lends it to be better described through statistics than through its exact details. Turbulence statistics include the mean, variance (or flux), skewness, and higher order moments. A common statistic employed in the ABL to describe the spatial structure of turbulence is the second order structure function

$$\Delta T_h^2 = [T(x+h) - T(x)]^2, \tag{4.1}$$

where T is the temperature measured at location x and h is a separation distance. Through dimensional analysis, Kolmogorov (1941) determined that within the inertial range, where turbulence is assumed to be homogenous (spatially stationary) and isotropic (independent of coordinate axis rotation), the mean square of velocity differences (extended by Obukhov (1949) to include temperature differences, ΔT_h^2) at separation distance h should scale as

$$\langle \Delta T(h)^p \rangle = C_p h^{\frac{p}{3}}, \tag{4.2}$$

where p is the order of the moment, and C_p are universal constants. In micrometeorology, when $p = 2$, C_2 is known as the temperature structure parameter, which acts as a proportionality factor in the power law relationship that describes the intensity of the variation (Wyngaard et al. 1971).

Estimation of C_2 in the boundary layer is used to determine turbulent fluxes through the relationship between C_2 and the dimensionless stability parameter $\zeta = z/L$, where z is the height above the surface and L is the Obukhov length (to be defined later) (Hartogenisis and de Bruin 2005). C_2 is also used to quantify the intensity of these fluxes (Bonin et al. 2015). Calculation of C_2 in the ABL has historically been approached through tower instrumentation (Wyngaard et al. 1971), but these measurements are not without limitations. A time series from a single instrument can be used to quantify the spatial structure of temperature fluctuation by invoking Taylor's (1938) frozen turbulence hypothesis but relies on an often non-validated assumption, and this approach does not allow for the vertical spatial structure to be characterized. Furthermore, towers are limited in their spatial extent and resolution. In situ measurements can also be obtained from manned aircraft (Thompson et al. 1978; Kunkel et al. 1980). However, manned aircraft are expensive to operate and cannot fly safely at altitudes near the ground where understanding energy exchange is critical.

The effect of temperature fluctuations on light and sound propagation in the atmosphere (Sreenivasan and Antonia 1997) has allowed for the use of remote sensing technologies to measure temperature and C_2 in the ABL. Scintillometers have been used over the last two decades

to measure temperature fluctuations and derive C_2 (Beyrich et al. 2012). These measurements are, however, path averaged over distances ranging from 100 m to 10 km (van den Kroonenberg et al. 2012, Wainwright et al. 2015). Furthermore, they are usually captured at a single altitude, making scintillometry not useful for vertical profiles of temperature fluctuation (Bonin et al. 2015). Quantifying C_2 through sodar measurements is a complicated procedure, often resulting in the presentation of uncalibrated data (Danilov et al. 2004; Bonin et al. 2015).

Recent technological advancements in small unmanned aircraft systems (sUAS) have allowed for the capture of spatial data in the ABL that can improve our understanding of the physical processes present (Jacob et al. 2018). A handful of studies have utilized sUAS for calculation of C_2 (and correspondingly, the scales where the exponent 2/3 is valid) in the ABL (van den Kroonenberg et al. 2012, Bonin et al. 2015, Wainwright et al. 2015, Braam et al. 2016, Platis et al. 2016, Platis et al. 2017). Most of these studies, however, estimated C_2 from data collected horizontally, either by utilizing a spiral ascent in a localized area (Bonin et al. 2015, Wainwright et al. 2015) or by long horizontal transects across heterogeneous terrain (van den Kroonenberg et al. 2012, Platis et al. 2017). In the case of the former, the authors note anomalous estimates of C_2 and attribute these anomalies to changes in surface roughness or surface thermal properties (van den Kroonenberg et al. 2012), although Platis et al. (2017) note the challenge of separating landscape effects from the natural variation inherent to turbulence.

Vertical profiles allow for isolating the effects of a varying landscape on estimated turbulence statistics while capturing data in the principal direction of heat and momentum transfer in the ABL. This makes vertical profiles a key sampling methodology for understanding the exchange of energy between the atmosphere and the earth's surface (Mayer 2012, Jacob et al. 2018). C_2, as an ABL statistic, should be a universal function of a stability parameter (Pahlow et al. 2001), and should not depend on surface conditions or time of day (Wyngaard et al. 1971). The above power law relationship (Equation 4.2) assumes that the energy dissipation rate in the turbulent cascade remains constant and the statistics of the flow are solely dependent on the

energy dissipation rate, a key assumption in the universality of C_2. However, random fluctuations to the energy inputs at the largest scales lead to an energy dissipation rate that is not constant and a value of C_2 that changes from flow to flow (Mathieu and Scott 2000).

Assessment of small-scale turbulence statistics such as C_2 are important as they speak to its universality (Streenivasan et al. 1997). Theoretically, this type of assessment can inform on not only temperature variation in the ABL, but may lead to insights on the velocity field (Shraiman and Siggia 2000) or other stochastic processes outside the realm of boundary-layer turbulence (Vassilicos 1995). Practically, universality of the small scale simplifies the statistics needed to better parameterize weather and climate models. Such models will be improved with higher resolution spatio-temporal data provided through collection via sUAS. In order to best deploy sUAS for weather observation, knowledge of the spatial variation of the measured quantity is paramount. For this purpose, the structure function (or variogram) is ideal for measuring the spatial variation of turbulent structures in the ABL. To that end, the objective of this study is to estimate C_2 from numerous temperature profiles at multiple locations and during various stability conditions to assess its universality. It is hypothesized that estimates of C_2 plotted as a function of the stability parameter z/L will follow a common curve, indicating a possible universal function. Given the chaotic nature of ABL turbulence, it is expected that there will be some scatter. Nevertheless, any anomalous estimates of C_2 will be discussed in the context of observed surface conditions during the time of the flights.

Theory

Regionalized Variables

A stochastic spatial model that can be used to represent a turbulent quantity in the ABL is

$$Z(x) = \mu + \varepsilon'(x) + \varepsilon'', \tag{4.3}$$

where μ is a structural component (stationary mean), $\varepsilon'(x)$, is spatially correlated variation and ε'' is an uncorrelated error component (Burrough et al. 2015). A spatial stochastic model exhibits

two key qualities: spatial autocorrelation and spatial stationarity. Most continuous phenomena in nature exhibit some degree of spatial autocorrelation. That is, measured values closer to one another are likely to be more similar than values measured at a distance, *h*, further apart. Stationarity, the second key attribute of the random function, implies that the mean of the random process is constant (i.e., does not depend on *h*) and the covariance, $cov[Z(x + h), Z(x)]$, exists and depends only on *h.*

In some circumstances, the assumption of stationarity may not be met, such as the case of the power law relationship described by Equation 4.2, in which the variation with distance is unbounded. Instead, the first-order difference $Z(x + h) - Z(x)$ may be substituted for the covariance. Then, the expected value of the first-order difference is 0

$$E[Z(x) - Z(x + h)] = 0. \tag{4.4}$$

and any variation resulting from *h*,

$$var[Z(x) - Z(x + h)] = 2\gamma h,$$

is known as the variogram $2\gamma(h)$ (Chiles and Delfiner 2012). The variogram is analogous to the structure function described by Obukhov (1949). At short distances, the variogram is able to filter the mean, but if $Z(x + h) - Z(x) \neq \varepsilon (x + h) - \varepsilon (x)$, where $\varepsilon (x)$ is the residual process, the stochastic function becomes

$$Z(x) = \mu(x) + \varepsilon(x), \tag{4.5}$$

where $\mu(x)$ is a linear function of one or more trend parameters (Chiles and Delfiner 2012).

Obukhov Length

The Obukhov length is a length scale frequently used in micrometeorology to characterize the relative influences of buoyancy and shear in the production of turbulent kinetic energy (Stull 1988). *L* is defined as

$$L = \frac{-\rho c_p T u_\tau^3}{\kappa g H}, \tag{4.6}$$

where ρ is the density of air at temperature T, c_p is specific heat capacity, u_τ is the friction velocity, g is gravitational acceleration, and H is the sensible heat flux. The von Kármán constant κ is also typically included (Dyer 1974). Obukhov (1946) assumed that the aforementioned parameters were comprehensive in describing turbulence in the ABL. Combining them through dimensional analysis resulted in only one parameter with the dimension of length, L (Foken 2005).

During the day under unstable conditions, when warm air near the surface rises, H is positive, resulting in negative L values. When H is negative, typically at night during stable conditions, L values are positive. Accurate measurements of u_τ and H are difficult to obtain, so L is often estimated from surface gradients of wind speed and temperature such as through the Richardson number

$$R_i = \frac{g\Delta z\Delta\theta}{\theta_1 \Delta u^2}, \tag{4.7}$$

where $\Delta\theta$ is potential temperature difference at two levels, Δu is wind speed difference at two levels and Δz is the difference in height from which the measurements were collected (Essa 1999). Businger et al. (1971) defined the relationship between L and R_i as

$$\zeta = \frac{\phi_m^2}{\phi_h} R_i \tag{4.8}$$

where ϕ_h is a universal function for heat exchange, ϕ_m is a universal function of momentum, and $\zeta = z/L$ where z is the mean height of the measurements used in Equation 4.7. The universal functions have been estimated using constants from Högström (1988),

$$\phi_h = \begin{cases} 0.95\left(1 - \dfrac{16z}{L}\right)^{-0.5} & \text{z/L} < 0 \\ \left(0.95 + \dfrac{8z}{L}\right) & \text{z/L} > 0 \end{cases} \tag{4.9}$$

$$\phi_m = \begin{cases} \left(1 - \frac{19.3z}{L}\right)^{-0.25} & z/L < 0 \\ \left(1 + \frac{6z}{L}\right) & z/L > 0, \end{cases}$$

requiring an iterative process to solve for ζ, which is considered a dimensionless stability parameter. Positive values of ζ indicate stable conditions and negative values indicate unstable conditions.

Experimental Design

Study Locations

Sampling was performed at six different Oklahoma Mesonet sites, each located in one of six ecoregions present in the State of Oklahoma (Figure 4.1). The Oklahoma Mesonet (hereafter, Mesonet) is a network of 120 automated weather monitoring stations across the state of Oklahoma. Measurements for a variety of meteorological variables are captured at various points along a 10-meter tower and averaged and recorded every 5 minutes. Measured variables include temperature (at 1.5 m and 9 m), relative humidity, pressure, wind speed (at 2 m and 10 m), and wind direction, among others (McPherson et al. 2007). Conducting flights near a Mesonet station is necessary for completing the study objectives as the towers are outfitted with the instrumentation to simultaneously record temperature and wind at two levels. This allows for the estimation of the Richardson number (Equation 4.7).

Mesonet sites are located such that they represent the physical characteristics of the largest area as possible (Brock et al. 1995). Sites are generally located away from irrigated sites and bodies of water. Additionally, sites are situated in areas that are relatively flat (slope < 5º) and are free from obstructions that would interfere with wind measurements such as forests (Brock et al. 1995), but in the southeastern portion of the state this could not be avoided at all locations.

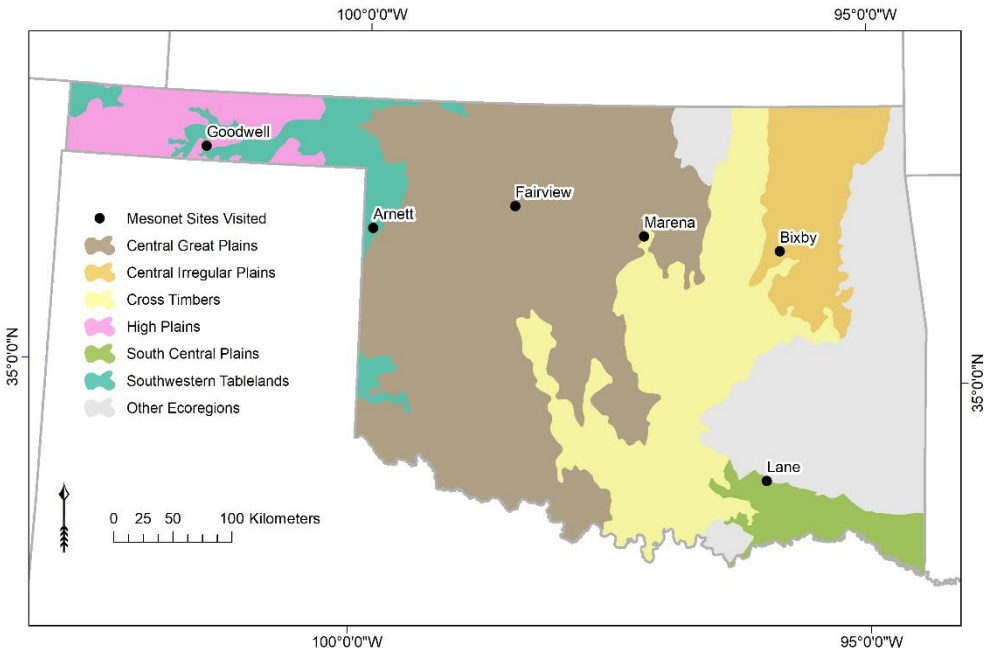

Figure 4.1. Oklahoma Mesonet sites and ecoregions visited.

The sites were selected in different ecoregions to capture a variety of environmental conditions. Ecoregions are biologically and geographically similar regions as designated by the United States Environmental Protection Agency (EPA) (Omernik 1987). Spatial patterns of land use, climate, soils, geology, and vegetation, among other characteristics, are compiled to delineate areas that are deemed similar. There are twelve Level III ecoregions in the State of Oklahoma. The names and general descriptions of the Mesonet sites visited are outlined below, and a brief description of the corresponding ecoregion is provided (Woods et al. 2005). Aerial photographs of the six Mesonet sites visited are presented in Figure 4.2.

- **Arnett** (36.072040°, -99.903080°) Elevation 719 m MSL. The Arnett site, located in the Southwestern Tablelands, is situated in an area of low hills with grassland and patchy, low trees. The Southwestern Tablelands are found in the Oklahoma panhandle. Vegetation consists of shortgrass prairie and sagebrush. The area is of high elevation

similar to the high plains and also experiences high winds and dramatic temperature changes.

- **Bixby** (35.963050°, -95.866210°) Elevation 184 m MSL. The Bixby site is located at Ringo Valley Agricultural Research Station. Located in a suburban area just north of the Arkansas River, the research station produces small grains, such as alfalfa and soybean. Extending into northwest Oklahoma, the Central Irregular Plains ecoregion is more topographically diverse than the Central Great Plains found further to the west. The central irregular plains separate the Cross Timbers region from the more heavily forested areas to the east, and as such are comprised of a forest/grassland mosaic.
- **Fairview** (36.263530°, -98.497660°) Elevation 405 m MSL. The Fairview site is located just off a two-lane road and near to a school grounds. Surrounding vegetation includes grasses, with few trees or other obstructions present. Located in the central great plains, the region is characterized by a semi-arid grassland prairie that makes up much of western Oklahoma. Tall grass and short grass prairie are present, but sand dunes, low mountains and salt flats are also found in the region. Winter wheat is a main crop in the farmland areas and rangeland can be found in areas of more rugged terrain.
- **Goodwell** (36.601830°, -101.601300°) Elevation 997 m MSL. The Goodwell site is located near a highway in a rural area consisting of low vegetation. Located in the high plains ecoregion, it is characterized by shortgrass prairie. High winds are frequent, as are dramatic shifts in temperature. The High Plains region of Oklahoma is also among the regions of the highest elevation in the state, exceeding 1000 m MSL.
- **Lane** (34.308760°, -95.997160°) Elevation 181 m MSL. The Lane site is located at the Lane Agricultural Center. Various vegetable crops are grown at the site. Rolling hills are present at the site, as are small stands of trees and a small pond. Located in the South Central Plains, the region is largely characterized by scrub oak woodland, as well as

coniferous forests. The climate is temperate and experiences more rainfall compared to other regions of the state.

- **Marena** (36.064340°, -97.212710°) Elevation 327 m MSL. The Marena site is located in an area of low, rolling hills with vegetation consisting of grasses and small stands of trees. The Cross Timbers ecoregion in central Oklahoma is comprised of both savannah and woodlands and act as a transition zone between the plains to the west and forests to the east. Various species of oak are present, as is red cedar. Fire suppression has largely contributed to the expansion of the latter.

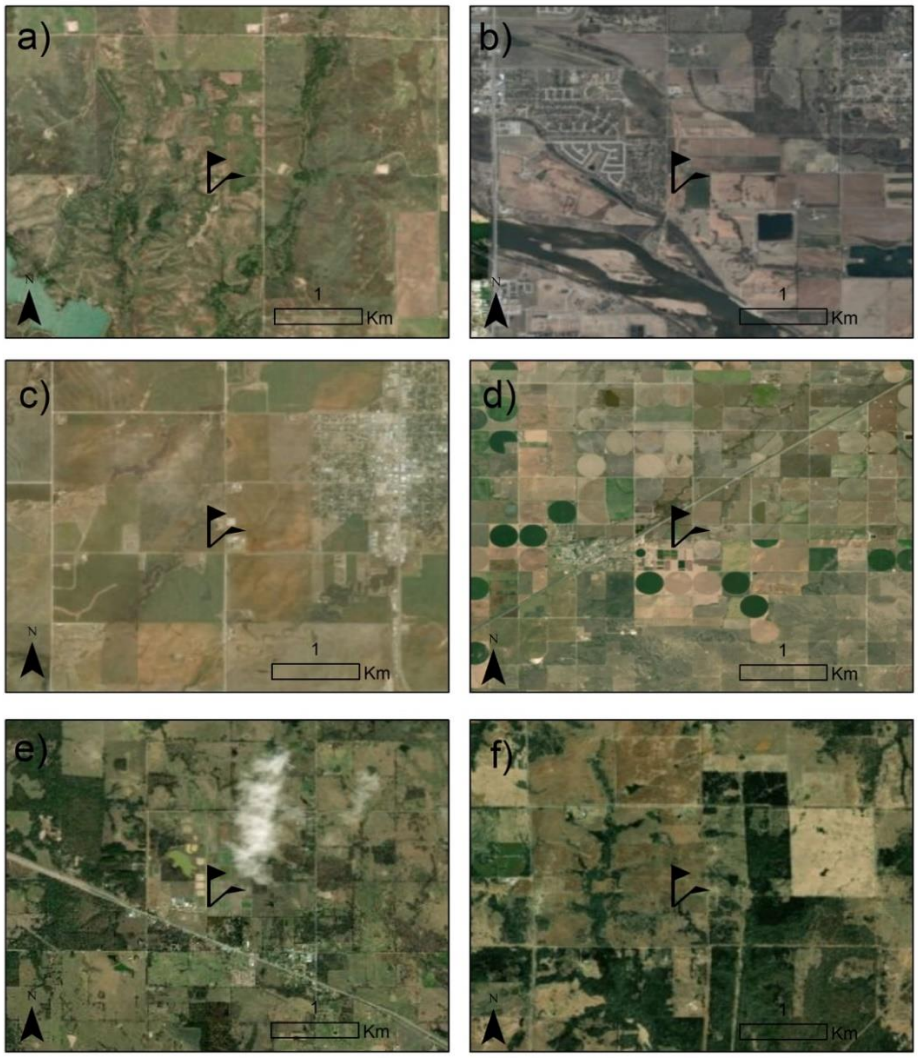

Figure 4.2. 1:50,000 aerial photos of the six Oklahoma Mesonet sites: (a) Arnett, (b) Bixby, (c) Fairview, (d) Goodwell, (e) Lane, and (f) Marena. Flag indicates location of Mesonet tower. (Imagery: ESRI)

Materials and Methods

Aircraft and Instrumentation

The sUAS used for data collections was a DJI Matrice 600 (DJI Shenzhen, Guandong, China). The hexacopter weighs 9.1 kg and is 1.13 m in diameter. Its 7 kg payload capacity was able to accommodate the placement of a R.M. Young Model 81000 (R.M. Young Company, Traverse City, MI) ultrasonic anemometer. Sonic temperature was collected at 32 Hz and synchronized to aerial telemetry and logged. The anemometer was mounted on the aircraft centrally above the rotors to minimize the effects of rotor downwash (Figure 4.3).

It is expected that some amount of measurement perturbation will occur with a rotor-wing platform. However, use of sonic temperature may be advantageous is this regard. Sonic temperature measured on an anemometer such as the one in this study is calculated using the transit time method (Brock and Richardson 2001). Sonic temperature is estimated through the calculation of the speed of sound, using the equation:

$$c = \frac{d}{2}\left(\frac{1}{t_1} - \frac{1}{t_2}\right), \tag{4.10}$$

where t_1 and t_2 are the transit times of an acoustic pulse between opposing transducers, respectively, d is the distance between the transducers, and c is the speed of sound. Sonic temperature, T, is then computed using the equation:

$$T = c^2 kR, \tag{4.11}$$

where k is the ratio of specific heat of air, and R is the specific gas constant. Since the speed of sound is independent of wind speed in the direction of the acoustic pulse, the vertical motion of the aircraft should have a negligible, if any, effect on the sonic temperature calculation.

Figure 4.3. R.M. Young Model 81000 ultrasonic anemometer with Oklahoma Mesonet tower in background. (Photo: Jamey Jacob).

Data Collection

Vertical profiles were flown in the immediate vicinity of the Mesonet tower. Between four and eight profiles were flown at each of the Mesonet sites visited and varied in time of day. All flights were conducted under the Federal Aviation Administration (FAA) Part 107 regulations, limiting the maximum altitude to ~122 m (400 ft.) above ground level (AGL) and also limiting flights to daylight hours. At some locations, flights were conducted throughout the morning ABL transition, whereas at other locations flights occurred in the afternoon. Flight times and summary statistics can be found in Table 4.1. Ascent speeds were roughly 3 m s^{-1}. Only data from the ascent was used in analysis to limit rotor wash interference and ensure greater temporal stationarity. Upon landing, logged data was downloaded from the flight control module and loaded onto a laptop for analysis. Surface measurements, including temperature at 1.5 m and 9 m, wind speed at 2 m and 10 m, and pressure, were downloaded from the Mesonet past data archive available online at mesonet.org.

Data Analysis Methods

Temperature residuals were separated from the mean profile through an ordinary least squares regression between temperature and height AGL. Residuals were then separated into bins based on their spatial separation distance from one another and sample variograms were estimated using the classic estimator:

$$2\hat{\gamma}(h) = \frac{1}{N(h)} \sum_{i=1}^{N(h)} \{Z(x_i) - Z(x_i + h)\}^2 , \tag{4.12}$$

where $Z(x_i)$ is the observed temperature residual at location x_i, $Z(x_i + h)$ is the observed temperature residual at location x_i separated by distance h, and N is the number of point pairs in each separation distance bin (Cressie 1993). Bin widths were set at 2 m, and the maximum separation distance at which point pairs were binned was set to 100 m. This was done to exclude the greatest separation distances where variogram estimates may be less reliable (Isaaks and Srivastava 1989).

Parameter estimation, including C_2 from Equation 4.2, was completed through fitting a model variogram to the estimated sample variogram. The power model variogram takes the form

$$2\gamma(h) = C_0 + C_2 h^{\alpha}, \tag{4.13}$$

where C_0 is an additive component allowing for a positive *y*-intercept (known as the nugget effect), and α is a scaling parameter. Following theory (Kolmogorov 1941; Obukhov 1949), α was fixed to 2/3, and C_0 and C_2 model parameters were estimated using non-linear least-squares. Variogram analysis was completed in the gstat package (Pebesma 2004) for the R statistical computing language.

The stability parameter z/L length was then estimated from Mesonet data of temperature and wind speed gradients. The Mesonet reports recorded measurements at 5-minute averages at 5-minute intervals. Mesonet records were selected such that the time span of the 5-minute average encompassed the majority of the flight time of the profile. For example, for Arnett Flight 1 (Table

4.1), the 7:40 record was obtained. The stability parameter z/L was then estimated using the equations outlined in Section 4.2. Estimates of C_2 were then plotted as a function of z/L to determine the universality of the relationship.

Site	Date	Flight #	Start Time	End Time	Mean Temp [°C]
Arnett	8-Apr	1	7:35:09	7:36:15	16.09
		2	8:15:20	8:16:26	16.39
		3	8:58:34	8:59:35	16.72
		4	9:59:42	10:00:46	20.60
		5	11:04:59	11:06:03	23.78
		6	12:28:39	12:29:51	25.73
Bixby	11-Apr	1	7:36:28	7:37:32	11.58
		2	8:14:30	8:15:37	10.83
		3	8:56:47	8:57:51	10.38
		4	9:42:18	9:43:26	10.71
		5	10:25:21	10:26:26	10.24
		6	11:14:29	11:15:30	11.14
		7	12:01:05	12:02:12	10.97
		8	12:56:08	12:57:11	12.59
Fairview	7-Apr	1	16:01:19	16:02:21	26.31
		2	16:45:11	16:46:16	26.60
		3	17:30:14	17:31:18	26.74
		4	18:15:35	18:16:38	26.65
Goodwell	9-Apr	1	7:36:21	7:37:35	15.24
		2	8:07:17	8:08:27	15.32
		3	8:42:54	8:44:00	15.91
		4	9:29:56	9:31:10	17.49
		5	10:46:07	10:47:16	22.05
		6	12:01:34	12:02:41	26.58
Lane	12-Apr	1	8:31:35	8:32:38	8.70
		2	9:08:48	9:09:52	10.03
		3	9:55:30	9:56:33	11.04
		4	10:58:50	10:59:57	12.97
		5	12:01:01	12:02:06	14.30
		6	13:01:43	13:02:52	16.47
Marena	4-Apr	1	8:19:21	8:20:30	17.18
		2	9:26:18	9:27:34	18.81
		3	10:40:33	10:41:38	19.45
		4	11:28:13	11:29:18	20.36

Table 4.1. Flight start and end times. All times local (UTC -5). Maximum altitude of all flights was 122 m AGL.

Results and Discussion

Variograms of Temperature Profiles

Thirty-four total profiles were conducted across the six Mesonet sites/ecoregions. Seven of the profiles were conducted in stable conditions, according to the corresponding z/L estimate being greater than zero and 27 profiles were conducted in unstable conditions. The periodic shape of the variograms estimated from most of the profiles collected during stable conditions suggests that squared temperature differences become increasingly dissimilar with distance until ~ 50 m, where the squared temperature differences begin to become increasingly similar until the maximum separation distance is reached (Figure 4.4a). This behavior indicates periodicity or an oscillatory process present in the spatial autocorrelation. Gravity waves are often observed in a stable boundary layer (Stull 1988), as are inertial oscillations and nocturnal low-level jets, all of which are possible explanations for the shape of the variogram estimated from most of the stable profiles. As these variograms did not depict a power law relationship with separation distance, no estimate of C_2 could be obtained, thus these data were excluded from further analysis. Sample variograms estimated from most profiles conducted in unstable conditions depicted a power law increase with distance (Figure 4.4b), allowing for C_2 to be estimated through the fitting of a power law model variogram (Equation 4.13).

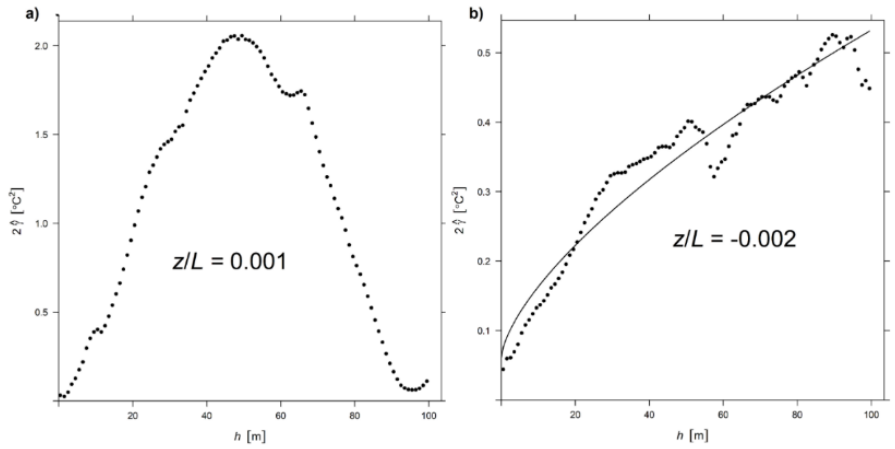

Figure 4.4. Sample variograms (points) from (a) Arnett Flight 1 during stable condition and (b) Goodwell Flight 3. Power law model variogram with α fixed to 2/3 fit to sample variogram.

The relationship between C_2 and z/L

Estimates of C_2 were plotted as a function of z/L (Figure 4.5) to determine if a universal relationship between the two parameters was present. A subset of points follow along a common curve, with C_2 estimates generally increasing as z/L increases towards neutral stability, with the highest C_2 estimates near $z/L = 0$. Points along the curve vary in both time of day and locations, suggesting that the relationship was not localized to a particular location or flow. There are several noticeable outlying observations that also vary in time of day and location. Flights 5 and 6 from Goodwell and Flights 2 and 5 from Lane have comparatively higher estimates of C_2 relative to their z/L estimate compared to observations along the common curve. There is also a cluster of several observations from different locations and times that have both a low C_2 estimate and a z/L estimate near zero.

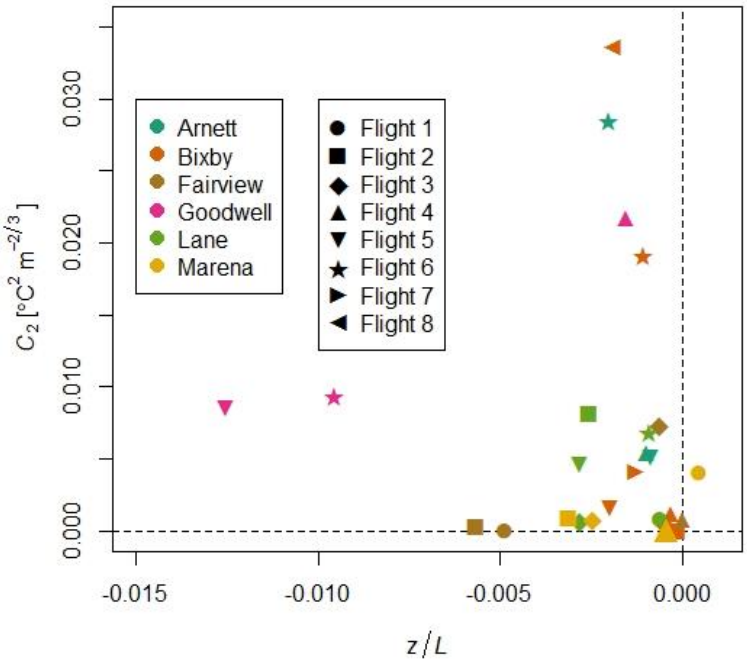

Figure 4.5. C_2 as a function of z/L.

Recall that positive values of *z*/*L* indicate stable conditions, and negative values indicate unstable conditions. Since height above ground, *z*, is always positive, the sign of *z*/*L* is determined by the sign of the Obukhov Length, *L*. When *L* is positive, turbulence is suppressed through static stability and results in a positive *z*/*L* value. When *L* is negative, the Obukhov length describes the relative contributions of mechanical forces (shear) and buoyancy in the production of turbulence. When *L* is negative and small, buoyancy dominates, and in turn, *z*/*L* is large and negative. When *L* is negative and large, shear is a greater contributor than buoyancy in turbulence production and *z*/*L* is negative and small. The results presented in Figure 4.5 suggest that the degree of temperature variation with vertical distance, as measured through C_2, increases as mechanical forces begin to dominate over buoyancy in the production of turbulence.

To situate the results in the context of the meteorological conditions present during the time of the profiles, meteograms of the conditions at all six Mesonet locations were created

(Figures 4.6–4.11). The cluster of potential outlier observations with C_2 and z/L estimates near zero (Figure 4.5) consists of Bixby Flights 1, 2, 3; Fairview Flight 4; Lane Flight 1; and Marena Flight 4. The meteograms (Figs. 4.7, 4.8, 4.9, 4.10, 4.11) depict the temperatures measured at 1.5 m and 9 m converge to a similar value at the time of these flights. This finding supports the low vertical temperature variation as assessed through the corresponding C_2 estimates. It is more challenging to draw any conclusions from the wind data about these particular six flights. During Bixby flights 1, 2, and 3 (Figure 4.8), the mean wind speed and maximum wind gust remained steady, while there was little change in wind direction. The meteogram for Fairview (Figure 4.9) depicts a slight drop in mean wind and wind gust during Flight 4. Conversely, wind speed increased slightly during Lane Flight 1 (Figure 4.10) and Marena Fight 4 (Figure 4.11). Wind direction during Lane Flight 1 shifted from NE to NW during the time of the flight (Figure 4.10).

Goodwell Flights 5 and 6 had higher C_2 estimates relative to their estimate of z/L (Figure 4.5). The mean temperature difference was ~1–2 º C cooler at 9 m than 1.5 m, indicating convective conditions (Figure 4.9). Wind gust and mean wind speed were increasing throughout the time period of Flights 5 and 6, but there was no measured spike in either. Fairview Flights 1 and 2, collected during the afternoon, should have been affected by convective turbulence, given their z/L estimates. However, the meteogram only depicts a slight decrease in temperature with height (< 1 º C), and mean wind and wind gust measurements display no anomalous spikes (Figure 4.8). Turning attention to the other end of the curve, Bixby Flights 6 and 8, Arnett Flight 6, and Goodwell Flight 4 (Figure 4.5) all had higher estimated C_2 relative to the other flights. Meteograms of Bixby Flights 6 and 8 (Figure 4.7) and Arnett Flight 6 (Figure 4.6) all depict a slight decrease in temperature (~1 º C) at 9 m compared to 1.5 m, indicating convective conditions. The corresponding z/L estimates for these flights is slightly greater than the estimates from flights with small negative z/L estimates along the common curve. These may be better described as outlier observations. Their higher C_2 estimates may be driven by convective, buoyant forces and not mechanical forces.

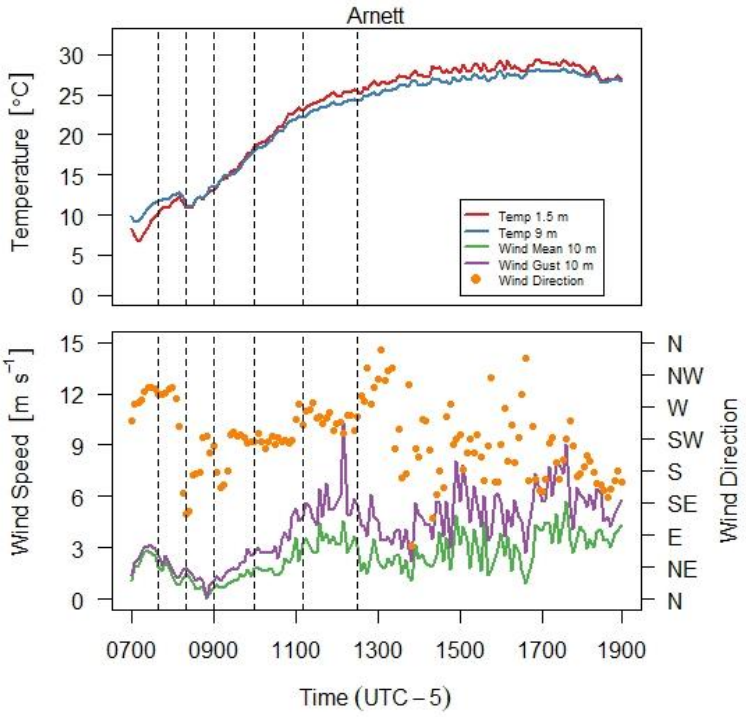

Figure 4.6. Meteogram of conditions at the Arnett site. Vertical dashed lines indicate flight times.

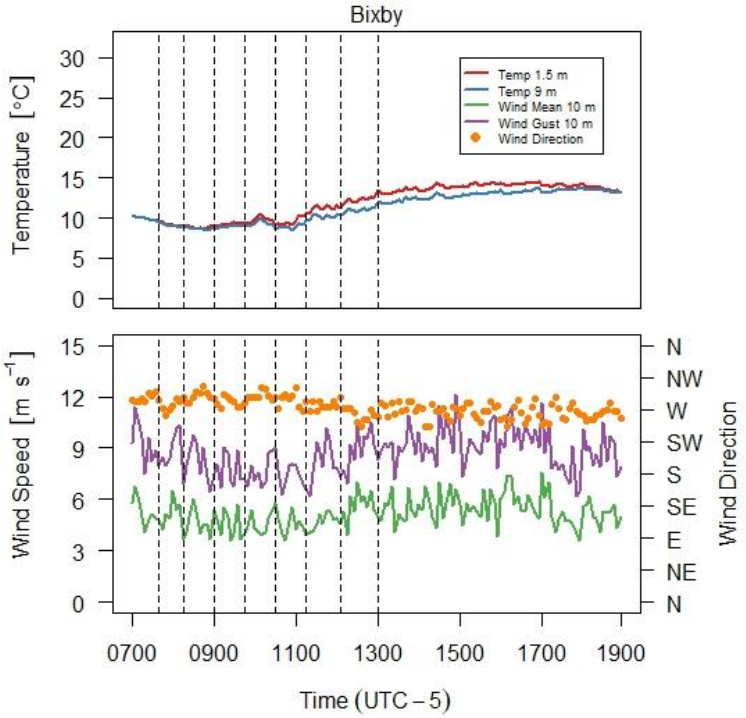

Figure 4.7. Meteogram of conditions at the Bixby site. Vertical dashed lines indicate flight times.

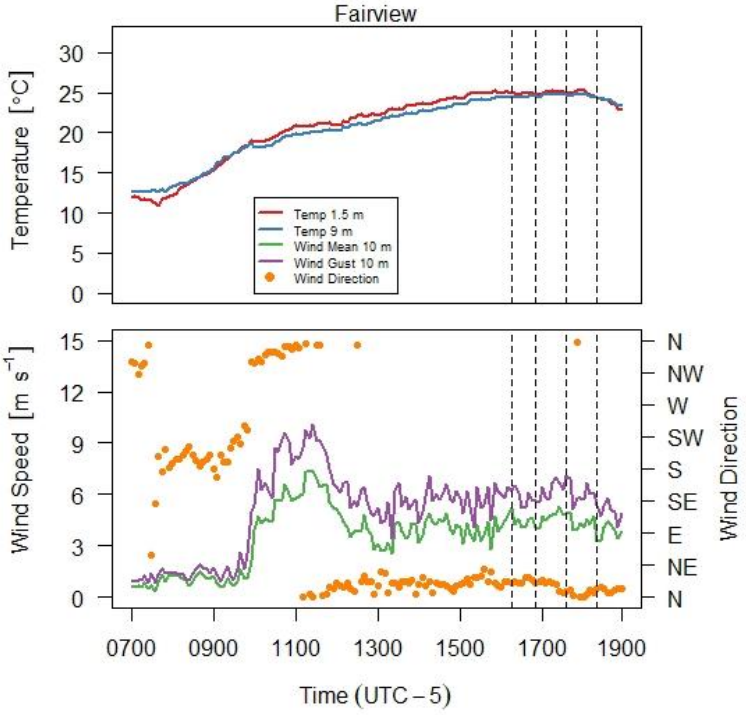

Figure 4.8. Meteogram of conditions at the Fairview site. Vertical dashed lines indicate flight times.

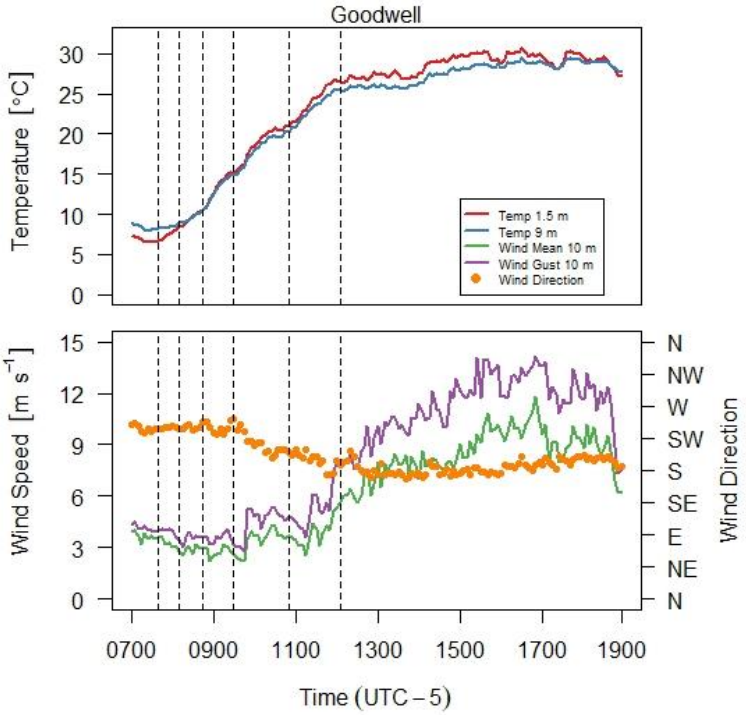

Figure 3.9. Meteogram of conditions at the Goodwell site. Vertical dashed lines indicate flight times.

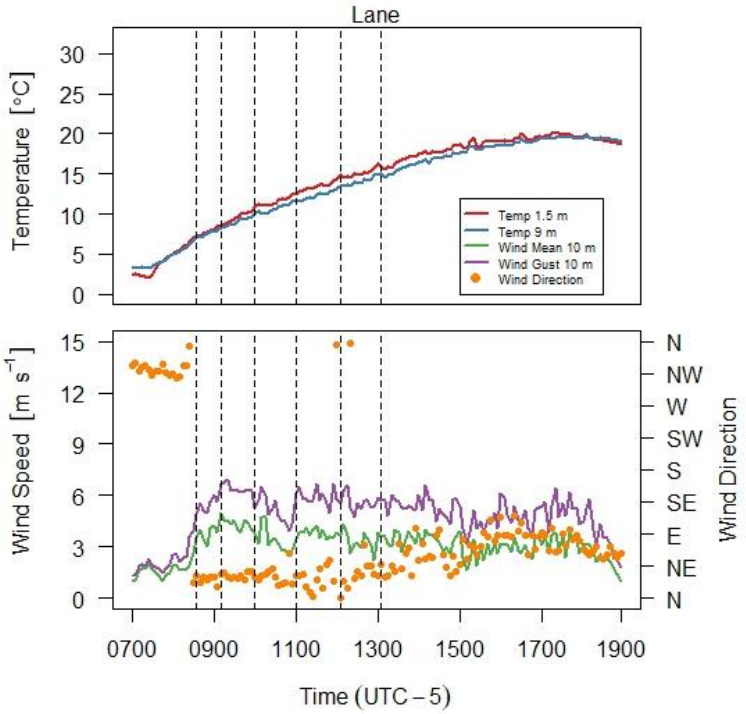

Figure 4.10. Meteogram of conditions at the Lane site. Vertical dashed lines indicate flight times.

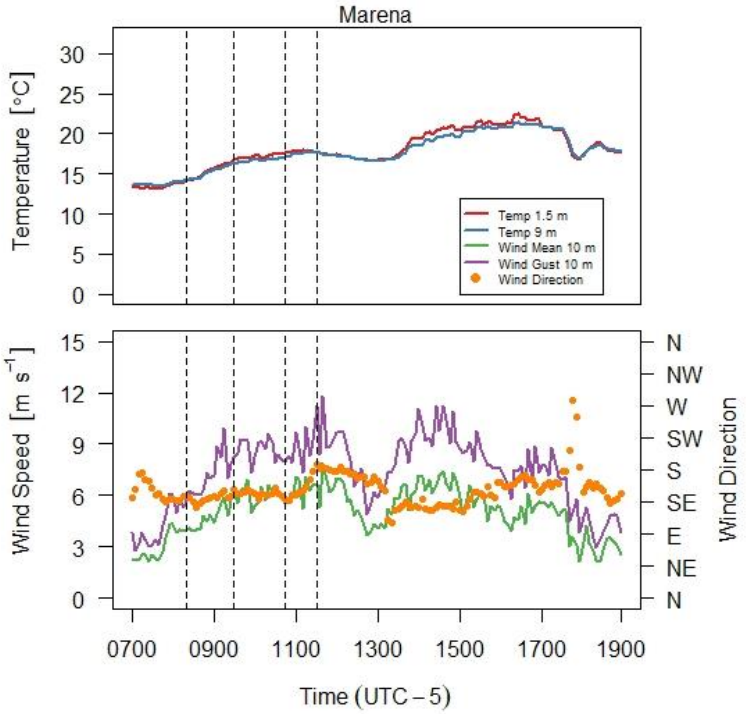

Figure 4.11. Meteogram of conditions at the Marena site. Vertical dashed lines indicate flight times.

Drawing definite conclusions from the data may be challenging, given the chaotic nature of ABL flows compared to those produced in a laboratory environment (Sreenvisan and Antonia 1997; Vindell et al. 2008). The results generally depict increasing vertical variation of temperature as shear increases. The exact cause of the anomalous C_2 estimates may not be able to be found with the data available. C_2 in Equation 4.2 is determined by the energy dissipation rate in the turbulent cascade. The dimensional analysis that led to the formulation of Equation 4.2 assumed that the mean energy dissipation rate remains constant and the statistical properties of the inertial range are independent of those of the larger, energy producing eddies (Sreenivasan and Antonia 1997), a key assumption of Kolmogorov's (1941) hypothesis. The lack of universality implies that the properties of the small scale are not independent. The inertial range is thus influenced by an energy dissipation rate that is not constant and/or the turbulent cascade is affected by other parameters. Thus, the lack of universality of the small scale is a result of intermittency of the large scale (Mathieu and Scott 2000).

Kolmogorov (1962) subsequently reformulated his theory at the suggestion of Obukhov (1962) to account for a spatially-varying energy dissipation rate. Though there is intermittency in the universality of C_2, it continues to be an important parameter in the calibration of remote sensing instruments (Wainwright et al. 2015) and estimation of surface fluxes used in parametrization of climate models and numerical weather prediction (Li et al. 2012). There was great scatter in the relationship between C_2 and z/L, and relatively high estimates of C_2 were observed at both ends of the observed z/L scale, suggesting an increase in C_2 as a result of both increased convection and mechanical shear. The cluster of C_2 estimates near the origin in Figure 4.5 may be the result of the spatial distance for which the structure function was calculated. Large scale intermittency in shear flows, such as a boundary layer, increases near the boundary of laminar/turbulent flow, leading to a decrease in C_p (Mathieu and Scott 2000). The particular profiles associated with the aforementioned anomalous C_2 estimates may have crossed such a boundary resulting in the intermittent intensity of C_2.

Conclusion

Multiple temperature profiles spanning varied stability conditions across six distinct ecoregions of Oklahoma were conducted to assess the universality of the second-order temperature structure parameter, C_2. Variograms from most profiles conducted in stable conditions did not exhibit the power law form necessary to estimate C_2. Most profiles conducted in unstable conditions had variograms that displayed the theorized power law relationship with distance. C_2 was estimated from these data through fitting a power law model variogram using non-linear least squares. Resulting estimates of C_2, were plotted as a function of the stability parameter z/L and were found to be scattered, though a subset of observations were found to follow a common curve. Outlying observations, varying in both location and time of day, were noted and hypothesized to be the result of large-scale intermittency in the turbulent cascade. Such intermittent variation in the temperature profiles was found to be well characterized by surface conditions and may change rapidly in time such that sUAS "snapshots" of temperature profiles and short-term averages of surface conditions may not fully capture the causes of the observed variation.

References

Beyrich, F., Bange, J., Hartogensis, O.K., Raasch, S., Braam, M., van Dinther, D., Gräf, D., van Kesteren, B., van den Kroonenberg, A.C., Maronga, B. and Martin, S., (2012). Towards a validation of scintillometer measurements: the LITFASS-2009 experiment. *Boundary-Layer Meteorology*, *144*(1), 83–112.

Bonin, T.A., Goines, D.C., Scott, A.K., Wainwright, C.E., Gibbs, J.A. and Chilson, P.B., (2015). Measurements of the temperature structure-function parameters with a small unmanned aerial system compared with a sodar. *Boundary-Layer Meteorology*, *155*(3), 417–434.

Braam, M., Beyrich, F., Bange, J., Platis, A., Martin, S., Maronga, B. and Moene, A.F., (2016). On the discrepancy in simultaneous observations of the structure parameter of temperature using scintillometers and unmanned aircraft. *Boundary-Layer Meteorology*, *158*(2), 257–283.

Brock, F. & Richardson, S. (2001). *Meteorological measurement systems*. New York: Oxford.

Brock, F.V., Crawford, K.C., Elliott, R.L., Cuperus, G.W., Stadler, S.J., Johnson, H.L., & Eilts, M.D. (1995). The Oklahoma Mesonet: a technical overview. *Journal of Atmospheric and Oceanic Technology*, *12*(1), 5–19.

Burrough, P.A., McDonnell, R., McDonnell, R.A., Lloyd, C.D. (2015). *Principles of Geographical Information Systems*, 3rd ed; Oxford University Press: New York.

Businger, J.A., Wyngaard, J.C., Izumi, Y., & Bradley, E.F. (1971). Flux-profile relationships in the atmospheric surface layer. *Journal of the atmospheric Sciences*, *28*(2), 181–189.

Cressie, N. (1993). *Statistics for spatial data*, New York, Wiley.

Danilov, S.D., Guryanov, A.E., Kallistratova, M.A., Petenko, I.V., Singal, S.P., Pahwa, D.R., & Gera, B.S. (1994). Simple method of calibration of conventional sodar antenna system. *Remote Sensing*, *15*(2), 307–312.

Dyer, A. (1974). A review of flux-profile relationships. *Boundary-Layer Meteorology*, *7*(3), 363–372.

Essa, K.S. Estimation of Monin-Obukhov Length Using Richardson and Bulk Richardson Number. *In Proceedings of the 2nd Conference on Nuclear and Particle Physics*, Cairo, Egypt, 13–17 November 1999.

Jacob, J.D., Chilson, P.B., Houston, A.L., & Smith, S.W. (2018). Considerations for atmospheric measurements with small unmanned aircraft systems. *Atmosphere*, *9*(7), 252.

Kunkel, K.E., Walters, D.L., & Ely, G.A. (1981). Behavior of the temperature structure parameter in a desert basin. *Journal of Applied Meteorology*, *20*(2), 130-136.

Högström, U.L.F. (1988). Non-dimensional wind and temperature profiles in the atmospheric surface layer: A re-evaluation. In *Topics in Micrometeorology. A Festschrift for Arch Dyer* (pp. 55-78). Springer, Dordrecht.

Hartogensis, O.K. (2005). Monin–Obukhov similarity functions of the structure parameter of temperature and turbulent kinetic energy dissipation rate in the stable boundary layer. *Boundary-layer meteorology*, *116*(2), 253–276.

Isaaks, E.H.; Srivastava, R.M. (1989). *Applied geostatistics*, Oxford, Oxford University Press.

Kolmogorov A.N., (1941). Local structure of turbulence in an incompressible fluid for very large Reynolds numbers. *Dokl. Akad. Nauk. SSSR*, *30*, 299–303.

Kolmogorov, A.N. (1962). A refinement of previous hypotheses concerning the local structure of turbulence in a viscous incompressible fluid at high Reynolds number. *Journal of Fluid Mechanics*, *13*(1), 82–85.

Li, D., Bou-Zeid, E., & De Bruin, H.A. (2012). Monin–Obukhov similarity functions for the structure parameters of temperature and humidity. *Boundary-layer meteorology, 145*(1), 45–67.

Mathieu, J, & Scott, J. (2000). *An introduction to turbulent flow*. Cambridge: Cambridge University Press.

McPherson, R.A., Fiebrich, C.A., Crawford, K. C., Kilby, J.R., Grimsley, D.L., Martinez, J.E., Basara, J.B., Illston, B.G., Morris, D.A., Kloesel, K.A. (2007). Statewide monitoring of the mesoscale environment: a technical update on the Oklahoma Mesonet. *J. Atmos. Ocean. Tech*. 24, 301–321.

Obukhov, A.M. (1946) 'Turbulentnost' v temperaturnoj – neodnorodnoj atmosfere (Turbulence in an Atmosphere with a Non-Uniform Temperature)', Trudy Inst. Theor. Geofiz. AN SSSR 1, 95–115.

Obukhov, A.M. (1949). Structure of the temperature field in turbulent flow. *Geogr. i Goofiz., 2*(1), 58–69.

Oboukhov, A.M. (1962). Some specific features of atmospheric turbulence. *Journal of Fluid Mechanics*, *13*(1), 77-81.

Omernik, J.M. (1987). Ecoregions of the conterminous United States. *Annals of the Association of American Geographers*, *77*(1), 118–125.

Pahlow, M., Parlange, M.B., & Porté-Agel, F. (2001). On Monin–Obukhov similarity in the stable atmospheric boundary layer. *Boundary-Layer Meteorology*, *99*(2), 225–248.

Pebesma, E.J. (2004). Multivariable geostatistics in S: the gstat package. *Computers & geosciences*, *30*(7), 683–691.

Platis, A., Altstädter, B., Wehner, B., Wildmann, N., Lampert, A., Hermann, M., ... & Bange, J. (2016). An observational case study on the influence of atmospheric boundary-layer dynamics on new particle formation. *Boundary-Layer Meteorology*, *158*(1), 67–92.

Platis, A., Moene, A.F., Villagrasa, D.M., Beyrich, F., Tupman, D., & Bange, J. (2017). Observations of the Temperature and Humidity Structure Parameter Over Heterogeneous Terrain by Airborne Measurements During the LITFASS-2003 Campaign. *Boundary-Layer Meteorology, 165*(3), 447–473.

Pope, S. (2000). *Turbulent flows*. New York: Cambridge University Press.

Richardson, L.F. (1922). *Weather prediction by numerical process*. New York: Cambridge University Press.

Sreenivasan, K.R. & Antonia, R.A., (1997). The phenomenology of small-scale turbulence. *Annual review of fluid mechanics*, *29*(1), 435–472.

Stull, R.B. (1988). *An introduction to boundary layer meteorology*. Dordrecht: Kluwer Academic Publishers.

Taylor, G.I. (1938) The spectrum of turbulence. *Proc R Soc London Ser A 164*: 476–490.

Thomson, D.W., Coulter, R.L., & Warhaft, Z. 1978. Simultaneous measurements of turbulence in the lower atmosphere using sodar and aircraft. Journal of Applied Meteorology, *17*(6), 723–734.

van den Kroonenberg, A.C., Martin, S., Beyrich, F. & Bange, J., (2012). Spatially-averaged temperature structure parameter over a heterogeneous surface measured by an unmanned aerial vehicle. *Boundary-layer Meteorology*, *142*(1), 55–77.

Vindel, J.M., Yagüe, C., & Redondo, J.M. (2008). Structure function analysis and intermittency in the atmospheric boundary layer. *Nonlinear Processes in Geophysics*, *15*(6).

Wainwright, C.E., Bonin, T.A., Chilson, P.B., Gibbs, J.A., Fedorovich, E. & Palmer, R.D., (2015). Methods for evaluating the temperature structure-function parameter using unmanned aerial systems and large-eddy simulation. Boundary-Layer Meteorology, *155*(2), 189–208.

Webster, R & Oliver, M.A., (2007). *Geostatistics for Environmental Scientists*. New York, Wiley.

Woods, A.J., Omernik, J.M., Butler, D.R., Ford, J.G., Henley, J.E., Hoagland, B.W., Arndt, D.S., & Moran, B.C., 2005, Ecoregions of Oklahoma (color poster with map, descriptive text, summary tables, and photographs): Reston, Virginia, U.S. Geological Survey.

Wyngaard, J.C., Izumi, Y., & Collins, S.A. (1971). Behavior of the refractive-index-structure parameter near the ground. *JOSA*, *61*(12), 1646–1650.

CHAPTER V

CONCLUSION

Summary

This doctoral dissertation research has used geostatistical tools, principally, variogram analysis, to describe the spatial structure of thermodynamic variables in the atmospheric boundary layer (ABL) using instrumentation deployed onboard small unmanned aircraft systems (sUAS). sUAS have emerged as a versatile platform from which to capture atmospheric measurements that have the unique ability to be deployed in such a manner that fills spatio-temporal gaps left by traditional sensing methodologies. While the technology to allow for the development of such platforms has advanced immensely in the last decade, the foundational knowledge on how to best sample physical processes in the ABL that are inherently spatial has received little attention. Historically, in situ sensing of the ABL and turbulent structures therein has been accomplished through tower instrumentation and the application of Taylor's (1938) frozen turbulence hypothesis. Sampling a domain in space is accompanied by its own set of challenges.

The variogram was originally conceived for such a purpose and the geostatistical theory developed in subsequent years in various other disciplines provides a framework that is well-suited to accommodate the non (spatially) stationary and seemingly chaotic nature of thermodynamic and other scaler variables in the ABL influenced by turbulent flows. This research has sought to combine small-scale turbulence theory and practical geostatistical

methodology with the dynamic data collection capabilities that are provided by sUAS. The preceding chapters have applied the aforementioned theory and methodology to provide insight into the spatial behavior of atmospheric variables that can inform deployment strategies for sUAS in the ABL.

In Chapter 2, variogram analysis was used to identify a methodology for identifying the smallest sampling scales necessary for capturing temperature and relative humidity measurements from an sUAS. Variograms displayed multiple peaks or plateaus of autocorrelation, suggesting that autocorrelation of the variable dissipates over a range of length scales. The range distance of the first plateau would thus correspond to the maximum distance one should sample in order to capture the smallest scale structures. It was found that optimal vertical sampling scales for the profiles analyzed were roughly 5 m for early morning flights. After the ABL became mixed, and conditions became unstable, a finer sampling scale of roughly 2 m would be necessary to capture the smallest autocorrelated structures. As the ABL became more turbulent (i.e., chaotic), autocorrelation decreased and the spatial positioning of a sample was influenced by a closer group of neighboring samples.

Similar autocorrelation behavior was observed in Chapter 3. Variograms were estimated from de-trended temperature profiles to account for the vertical nonstationarity of temperature with respect to height in the ABL. It was observed that the power law behavior of squared temperature residuals increased at a rate steeper than theorized in the variograms estimated from early-morning profiles. A power law variogram displaying such behavior is indicative of a more deterministic process than a power law variogram that appears flatter. As a result, temperature profiles predicted using the theorized 2/3 power law model variogram were under predicted in the early morning, whereas late morning/early afternoon profiles conformed more closely to the theorized scaling relationship. Consequently, the inertial range of turbulence scale was able to be resolved at various separation distances and heights AGL for the three profiles conducted under

well mixed conditions. Chapter 3 was also successful in demonstrating the ability of geostatistics to accommodate nonstationary random variables.

In Chapter 4, the universality of the temperature structure parameter, a proportionality factor in the 2/3 power law relationship, was assessed through multiple flights across a variety of Oklahoma ecoregions and times of day. The 2/3 power law scaling investigated in Chapter 3 is a result of dimensional analysis and its validity relies on a number of assumptions. Particularly, it is assumed that the energy dissipation rate is the only variable influencing the eddies as energy cascades from the largest scales to the smallest scales, and that the energy dissipation rate remains constant. A result of these assumptions is that the temperature structure parameter, C_2, should be a universal function of a stability parameter. A general relationship between C_2 and the stability parameter z/L was observed, with deviations observed from multiple locations and flight times. While there was a general relationship, the exact cause for the anomalies could not be identified with the data available.

This research has demonstrated that once the ABL becomes unstable and experiences vertical mixing, the spatial discontinuity of random thermodynamic random variables increases resulting in the need for increased spatial sampling frequency. The results have also demonstrated that at medium separation distances, the theorized scaling is valid as the ABL becomes more turbulent and was validated at altitudes up to 500 m AGL. The statistics of the flow in turbulent conditions are generally a universal function of a stability parameter, though variability was demonstrated to be at times intermittent. This intermittency was observed during periods of increased turbulence contributions of both convection and shear and varied in time on scales of less than 1 hour. This suggests that to capture thermodynamic variation, increased temporal frequency of profiles would likely be beneficial.

Limitations and Future Considerations

There remains much to be understood about how to best sample the ABL with sUAS. A chief point of concern is not only the minimum sampling distance as discussed in Chapter 2, but

the maximum sampling distance, or more precisely, the size of the sampling domain. The maximum separation distance for which the variogram is estimated will have an effect of the variogram estimates therein. The spatial measurements captured by sUAS are taken on finite profiles (or transects), which limit the effective variation that can be detected. At medium distances, temperature variation displays a power law relationship with separation distance, as demonstrated in Chapters 3 and 4. The power law model variogram is unbounded, meaning it does not reach a sill or a limit to its variation. Hence, variation may increase beyond the finite region of our sampling profile. Statistics computed from a 122 m profile (the current legal AGL limit in the U.S.) may not be fully representative of the full boundary layer.

At greater maximum separation distances, the variogram ma reach a sill, as was observed by Hemingway and Frazier (2018), albeit with horizontal transects. When technology and the law allow for sUAS profiles of the full depth of the ABL, a variogram such as the stable model might be appropriate for parameterizing temperature structure. The stable modal has a scaling exponent, like the power model, but has the advantage of reaching a sill (Chiles and Delfiner 2012). Until the time when full profiles of the ABL can be routinely captured, the knowledge of how statistics from 100 m profiles scale to what would be captured with a greater spatial sampling domain would be beneficial.

While spatial stationarity is a key condition to geostatistical and turbulence, a related concept called ergodicity is likewise important. A random process is said to be ergodic if the statistical moments of a spatial subset of a single realization of the random function are equal to that of the ensemble average (Cressie 1993; Webster and Oliver 2007). The theory is mostly relevant to time series and is considered to be of only theoretical importance in geostatistics (Webster and Oliver 2007). It becomes an important concept, however, when thinking about how we may best sample the atmosphere. Much of the theory of physical processes in the atmosphere is based on ensemble averages; after all, the ABL has been predominately sampled in the temporal domain. Since eddies in the ABL scale roughly to the ABL thickness and the largest

structures are influenced by the mean wind, the largest structures (i.e., the full extent of the variability of that particular realization) can be determined, and is done so routinely through the calculation of the integral scale of turbulence. Short term averages, spatial or temporal, are not likely to be representative of the ensemble averages (Wyngaard et al. 1971), resulting in observed variability that is intermittent.

Intermittency is a phenomenon that has received considerable attention in turbulence literature (Monin and Yaglom 1975). Not only is there intermittency in the large scales, as discussed in Chapter 4, but there is also intermittency in the small scales (i.e., the inertial range) (Mathieu and Scott 2000). Small-scale intermittency is predominately studied through analysis of the inertial range scaling exponents and their deviation from the theorized relationship (Equation 3.1). However, it is noted that the scatter present in ABL data makes precise quantification of intermittency challenging in the temporal domain (Vindel et al. 2008). Applying the same theory to quantify intermittency spatially will likely be correspondingly difficult. Separating intermittent variability from variability present as a result of a finite spatial average will be an important avenue of future research.

Concluding Remarks

sUAS are increasingly becoming a valuable sensing tool in the ABL. As more data is collected in the spatial domain, consideration should be given as to how to best collect and analyze the data. Statistics are well suited for description of ABL processes given their chaotic, seemingly random behavior. Geostatistics, thus, is a viable toolkit for estimating nonstationary means, fitting models to describe the structure of the errors, and estimating values at unsampled locations. Geostatistics is rooted in the theory of turbulence. Combined with the sampling capabilities of sUAS, geostatistics can be applied to better understand the ABL and the physical processes within it that affect so much of our daily lives on Earth.

References

Chiles, J-P, & Delfiner, P. (2012) Geostatistics: modeling spatial uncertainty. New York: Wiley.

Cressie, N. (1993). *Statistics for spatial data*. Hoboken, NJ: Wiley.

Hemingway, B.L. and Frazier, A.E. (2018) Geostatistical detection of thermodynamic anisotropy in an atmospheric boundary layer using small unmanned aircraft systems. *Proceedings of the 21st Association of Geographic Information Laboratories of Europe Conference*. Lund, Sweden.

Mathieu, J, & Scott, J. (2000). *An introduction to turbulent flow*. Cambridge: Cambridge

Monin, A.S. & Yaglom, A.M. (1975). *Statistical fluid mechanics*. Cambridge: MIT Press.

Taylor, G.I. (1938) The spectrum of turbulence. *Proc R Soc London Ser A 164*: 476–490.

Vindel, J.M., Yagüe, C., & Redondo, J.M. (2008). Structure function analysis and intermittency in the atmospheric boundary layer. *Nonlinear Processes in Geophysics*, *15*(6).

Webster R. & Oliver M.A. (2007). *Geostatistics for environmental scientists*. New York: Wiley.

Wyngaard, J.C., Izumi, Y., & Collins, S.A. (1971). Behavior of the refractive-index-structure parameter near the ground. *JOSA*, *61*(12), 1646–1650.

VITA

Benjamin Lynn Hemingway

Candidate for the Degree of

Doctor of Philosophy

Thesis: GEOSTATISTICAL ANALYSIS OF TEMPERATURE STRUCTURE IN THE ATMOSPHERIC BOUNDARY LAYER

Major Field: Geography

Biographical:

Education:

Completed the requirements for the Doctor of Philosophy in Geography at Oklahoma State University, Stillwater, Oklahoma in May, 2020.

Completed the requirements for the Master of Science in Geography at Oklahoma State University, Stillwater, Oklahoma in 2016.

Completed the requirements for the Bachelor of Arts in Geography at University of Arizona, Tucson, Arizona in 2010.

Experience:

Research Technician, Lunar Reconnaissance Orbiter Camera, Arizona State University, Tempe, Arizona, 2019–Present

Graduate Research Associate, Department of Geography, Oklahoma State University, Stillwater, Oklahoma, 2016–2019

GIS Intern, Chesapeake Energy Corporation, Oklahoma City, Oklahoma, 2015

Graduate Teaching Assistant, Department of Geography, Oklahoma State University, Stillwater, Oklahoma, 2014–2015

Professional Memberships:

American Geophysical Union

International Society for Atmospheric Research using Remotely-piloted Aircraft